Applied Catalysis B: Environmental 291 (2021) 120056

Contents lists available at ScienceDirect

Applied Catalysis B: Environmental

journal homepage: www.elsevier.com/locate/apcatb

Visible-light-driven lanthanide-organic-frameworks modified TiO_2 photocatalysts utilizing up-conversion effect

Patrycja Parnicka [a], Wojciech Lisowski [b], Tomasz Klimczuk [c], Justyna Łuczak [d], Andrzej Żak [e], Adriana Zaleska-Medynska [a,*]

[a] Department of Environmental Technology, Faculty of Chemistry, University of Gdansk, 80-308, Gdansk, Poland
[b] Institute of Physical Chemistry, Polish Academy of Sciences, 01-224, Warsaw, Poland
[c] Faculty of Applied Physics and Mathematics, Gdansk University of Technology, 80-233, Gdansk, Poland
[d] Department of Process Engineering and Chemical Technology, Faculty of Chemistry, Gdansk University of Technology, 80-233, Gdansk, Poland
[e] Electron Microscopy Laboratory, Faculty of Mechanical Engineering, Wroclaw University of Science and Technology, 50-372, Wroclaw, Poland

ARTICLE INFO

Keywords:
Lanthanide-organic frameworks
Metal-organic frameworks
Titanium dioxide
Visible light photoactivity
Up-conversion

ABSTRACT

Highly efficient and quite stable composite with core-shell-like architecture reported herein, responds to the challenge of sunlight-driven photocatalysts. The Ln(ndc)/TiO_2 photocatalytic system comprises active lanthanide-carboxylate coordination networks (Nd, Er, Ho, and Tm as metal ions, and 2,6-naphthalene dicarboxylic acid as the organic linker) and inert titanium dioxide and allow to convert incompatible visible radiation into functional ultraviolet photons. The combination of the antenna-reactor photocatalyst complex with Ln(ndc) shell layers promotes light harvesting and efficient mass transfer, resulting in additional photoexcited electrons. The Nd(ndc) metal-organic framework successfully activate TiO_2 *via* up-conversion energy transfer. The apparent quantum efficiency, determined at wavelengths corresponding to the transitions from the Nd^{3+} ground state, equals to 2.8% and 3.2% for 525 and 583 nm, respectively. Integration of the Nd(ndc) MOF and TiO_2 results in the highest efficiency of phenol degradation, affording a value of 87.5% after 60 min of visible light ($\lambda > 420$ nm) exposure.

1. Introduction

Owing to the current energy and environmental issues, there is a large demand for the efficient use of renewable energy. Among the most promising renewable energy sources, solar energy is free, pure, and unlimited. Photocatalysis, which converts solar energy into chemical energy, is a promising approach to meet the current and future energy requirements. Considering that 92% of the solar spectrum corresponds to visible and infrared light, photocatalyst modification to achieve effective light absorption is one of the most challenging goals in heterogeneous photocatalysis [1].

In the field of photocatalytic degradation of contaminants, lanthanide-modified TiO_2 photocatalysts have attracted significant attention [2,3]. Owing to the unique properties of lanthanide ions, these show excellent potential as modifiers, not only because of the possibility of promoting absorption redshift and improving the adsorption ability, but also because of excellent energy transfer capability by converting low-energy photons into high-energy photons *via* the anti-Stokes process [4]. Based on the TiO_2 band structure, the wavelength range of Ln^{3+} energy transfer should allow the conversion of visible to UV light to act as a sensitizer. Although numerous studies have been performed on Ln^{3+}-modified TiO_2, only a few of these have investigated the effect of the up-conversion (UC) process on photocatalytic activity. The results indicate that Er^{3+}, Ho^{3+}, Nd^{3+}, and Tm^{3+} can be theoretically employed to sensitise TiO_2, and the UC process is not responsible for photocatalytic activity under visible light irradiation because of the low intensity of Ln^{3+} emission [5–8]. The luminescence of Ln^{3+} species is highly susceptible to the local crystal field environment. In particular, the 5d–4f transitions of lanthanide ions are significantly affected (both position and intensity) by the crystal field of the matrix. In some host matrices, the luminescence of Ln^{3+} increases considerably with an increase in crystallinity. Rare-earth ions (RE^{3+}) have large ionic radii (Sc^{3+} being the sole exception) and thus require high coordination, usually featuring high coordination numbers and connectivity. Therefore, RE^{3+}-modification of TiO_2 creates a charge imbalance and vacancies, which significantly affect the luminescence yield. However, high

* Corresponding author.
E-mail address: adriana.zaleska-medynska@ug.edu.pl (A. Zaleska-Medynska).

https://doi.org/10.1016/j.apcatb.2021.120056
Received 4 January 2021; Received in revised form 9 February 2021; Accepted 21 February 2021
Available online 28 February 2021

connectivity facilitates the formation of stable three-dimensional (3D) networks. The growth of lanthanide coordination and organometallic chemistry during the last several decades has resulted in numerous successful applications in catalysis [9], magnetism [10,11], biomedical analysis [12], diagnostic and therapeutic medicine [13,14], and luminescence [15].

Considering the above discussion, the subclass of metal-organic frameworks (MOFs), i.e., lanthanide-organic frameworks (LnOFs), as crystalline porous materials with diverse and tailorable structures can be good candidates for practical applications because of their suitable environments for luminophores in the crystalline state and characteristic optical performances. MOFs are valuable luminescence materials because both inorganic and organic parts participate in the generation of luminescence. This process effectively increases the luminescence quantum yield of Ln^{3+}. Numerous research groups have used 2,6-naphthalene dicarboxylic acid (2,6-ndc) as an organic linker owing to its multifunctional oxygen-donor connector with multiple chelating modes and the potential to form rigid framework structures, affording a high 2,6-ndc coordination capacity. Similar to other MOFs, LnOFs are also valuable luminescence materials as both inorganic and organic parts participate in luminescence generation [16]. For instance, Mahata et al. [17,18] prepared an Nd-based MOF using $[Nd_2(H_2O)(m\text{-}bdc)_2(m\text{-}Hbdc)_2]\cdot H_2O$ and $Nd_2(H_2O)_4(pdca)_2(p\text{-}BDC)$ with UC luminescent properties. The emission spectrum showed three peaks at approximately 364, 422, and 431 nm, corresponding to the $^4D_{3/2}\rightarrow{}^4I_{11/2}$, $^4D_{3/2}\rightarrow{}^4I_{13/2}$, and $^4D_{3/2}\rightarrow{}^4I_{15/2}$ transitions, respectively, upon excitation at 580 nm. Weng et al. [19] synthesised three new LnOFs ($[(Y: Er, Yb)(pza)(OH)\cdot(H_2O)]_n$) exhibiting UC properties with green and red emissions upon excitation at 975 nm. This corresponded to the two-photon excitation of the Y: Er, Yb co-doped coordination polymer and Eu^{3+} transitions of $^4S_{3/2}\rightarrow{}^4I_{15/2}$, $^2H_{11/2}\rightarrow{}^4I_{15/2}$, and $^4F_{9/2}\rightarrow{}^4I_{15/2}$. Yang et al. [20] developed a neodymium-coordinated polymer with general formula $Nd_2(1,4NDC)_3(DMF)4\cdot H_2O)$, which also showed UC properties with Vis-to-Vis and Vis-to-UV luminescence upon excitation with a 580-nm tunable pulsed laser, corresponding to the $^4I_{9/2}\rightarrow{}^4G_{5/2}$ transition of Nd^{3+}. It exhibited blue emission at approximately 450 nm and UV UC at approximately 391 nm.

Lanthanide-carboxylate coordination networks based on naphthalene dicarboxylate ligands are important for designing a unique platform for Vis-to-UV conversion by Ln-MOFs. For the first time, novel broadband-spectrum-responsive MOF composites with core-shell-like architectures, i.e., TiO_2/lanthanide-carboxylate coordination networks (LnOF = Nd, Er, Ho, and Tm as metals, and 2,6-ndc as an organic linker) that capture UV and Vis photons based on UC are reported in this study. To elucidate a possible excitation mechanism under visible light irradiation, the action spectra were obtained for phenol photodegradation. To determine the types of active species that participate in the degradation mechanism, photodegradation experiments in the presence of a scavenger and the hydroxyl radical test with terephthalic acid were performed. Diffuse reflectance spectroscopy (DRS), powder X-ray diffraction (pXRD), Fourier-transform infrared (FTIR) spectroscopy, X-ray photoelectron spectroscopy (XPS), scanning electron microscopy (SEM), transmission electron microscopy (TEM), thermogravimetric analysis (TGA), Brunauer–Emmett–Teller (BET) surface area measurements, and photoluminescence (PL) analysis were performed.

2. Experimental

2.1. Experimental details

2.1.1. Materials

All chemicals were purchased from Sigma-Aldrich (Germany), POCh S.A (Poland) and STANLAB (Poland), and used without further purification.

2.1.2. Preparation of hollow TiO_2 spheres

TiO_2 spheres were synthesised by the precipitation method, following a previously reported procedure [21]. Aqueous ammonia solution (0.342 mL) and deionised water (0.828 mL) were added to a mixture of ethanol and acetonitrile (6:4 (v:v); 250 mL). Then, titanium isopropoxide (5 mL) was promptly added to the above solution with vigorous stirring for a minimum of six hours. The formed TiO_2 spheres were centrifuged and washed with ethanol and water (three times each) to remove the unreacted precursor. Finally, the powders were calcined at 450 °C for two hours (2 °C/min).

2.1.3. Preparation of carboxylate TiO_2 spheres

Succinic anhydride (0.45 g) was dissolved in *N,N*-dimethylformamide (DMF, 30 mL), and (3-aminopropyl)triethoxysilane (APTES, 1 mL) was gradually added. After the mixture was stirred for three hours at room temperature, deionised water (2 mL) and the suspension of the hollow TiO_2 particles in DMF (10 mL, 0.05 g/mL) were added. The mixture was stirred for an additional eight hours. The product was then washed several times with ethanol and collected by centrifugation.

2.1.4. Preparation of TiO_2/LnOF and LnOF

The required amount of carboxylate-terminated TiO_2 (TiO_2_COO^-) was dissolved in DMF (100 mL), and neodymium nitrate, erbium nitrate, holmium nitrate, thulium nitrate, and 2,6-ndc acid (3:5 mmol molar ratio) were added to the mixture. The resulting mixture was stirred for approximately one hour at room temperature, sealed in a 200-mL Teflon-lined stainless-steel autoclave, and heated at 95 °C for three days under autogenous pressure. Subsequently, the reaction system was gradually cooled to room temperature. The as-prepared powder was collected from the final reaction system by filtration, washed several times with DMF and ethanol, and dried in air at 60 °C. LnOF was synthesised according to the procedure described above without TiO_2 addition. The mass percentages of LnOF in the composite were set to 15, 25, and 50 wt.% based on the ratio between the masses of the LnOF precursors and TiO_2 used in the synthesis.

2.2. Characterization techniques

The pXRD studies were performed on powdered samples using a Bruker D8 Advance Eco diffractometer with Cu Kα radiation and a LynxEye-XE detector. The lattice parameters of TiO_2 (anatase) were obtained employing the LeBail method using the FullProf package. FTIR spectroscopy was used to collect the spectra of the semiconductors in the scan range of 400–4000 cm^{-1} in the diffuse reflectance mode with a resolution of 8 cm^{-1} at room temperature using a Nicolet iS10 FTIR spectrometer. The samples were prepared by diluting 10% of the photocatalyst in KBr. XPS was used to investigate the surface chemical compositions of the prepared photocatalysts. A PHI 5000 VersaProbe (ULVAC-PHI, Chigasaki Japan) spectrometer with monochromatic Al Kα radiation ($h\nu$ =1486.6 eV) was used. The high-resolution (HR)-XPS spectra were recorded using a hemispherical analyser at a pass energy of 23.5 eV and an energy step size of 0.1 eV. The binding energy (BE) scale of all the recorded spectra was referenced by setting the BE of the carbon (C–C) signal to 284.8 eV. For quantification, the PHI Multipak sensitivity factors and transmission function of the spectrometer were used. The BET surface areas and pore sizes of the photocatalysts were measured using a Micromeritics Gemini V200 Shimadzu instrument equipped with a Vac Prep 061 Degasser. All samples were degassed at 200 °C prior to the nitrogen adsorption measurements. The BET surface area was determined using the multipoint BET method by employing the adsorption data in the relative pressure (P/P0) range of 0.05–0.3. TGA was performed using SDT Q600 (TA Instruments, USA) in a nitrogen atmosphere at a heating rate of 10 °C/min over a temperature range of 30–800 °C. The morphologies of the as-prepared samples were investigated using field-emission SEM (JSM-7610 F, JEOL), and TEM (H-800, Hitachi). To characterise the photo-absorption properties of the bare and

modified photocatalysts, the DRS data were obtained using a Shimadzu UV–vis spectrophotometer (UV 2600) equipped with an integrating sphere. $BaSO_4$ was used as the reference. The obtained absorption spectra were recorded at 250–850 nm and a scanning speed of 200 nm/min at room temperature. PL properties were determined in the 300–700 nm range using an LS50B spectrophotometer (Perkin Elmer Ltd.) equipped with a xenon discharge lamp as the excitation source and an R928 photomultiplier as the detector. The spectra were recorded at an excitation wavelength of 315 nm directed toward the sample surface at an angle of 90°.

2.3. Measurement of photocatalytic activity

2.3.1. Phenol degradation under visible light (polychromatic irradiation)

The photocatalytic performances of Ln(ndc)-modified TiO_2 samples for phenol degradation under visible light irradiation were investigated using a 1000 W xenon lamp (Oriel 66021) equipped with a 420-nm cut-off filter and water IR cut-off filter with constant aeration (5 dm^3/h). The temperature in the reactor during the process was maintained at 10 ± 0.5 °C using a thermostatically controlled water bath. The experiments were performed at initial phenol and photocatalyst concentrations of 0.21 mM and 5 g/L, respectively. The reaction mixture was added to the photoreactor, mixed for 10 min using an ultrasonic bath, and then stirred for additional 30 min. Thereafter, visible light irradiation was performed. Phenol solution (~0.5 mL) was retrieved at specific time intervals, filtered using a 0.2 μm syringe filter, and analysed. A high-performance liquid chromatography system (HPLC, Shimadzu) equipped with a Kinetex C18 column, a pre-column, and an SPD-M20A diode array detector (λ = 205, 225, and 254 nm) was used to determine the concentrations of phenol and the intermediates in the solution. The mobile phase was composed of acetonitrile and 0.005% trifluoroacetic acid, and isocratic elution (20:80 (v:v)) was used with a constant flow rate of 0.05 mL/min. The injection volume was 20 μL.

Determination of radical scavenging activity and hydroxide radicals (polychromatic visible irradiation)

Radical scavenging experiments to elucidate the potential role of the active species generated during heterogeneous photocatalysis were performed using benzoquinone, silver nitrate, ammonium oxalate, and tert-butanol. The phenol aqueous solution containing the above-mentioned scavengers (C_0 = 0.21 mM, 1:1) and photocatalyst was subjected to the same experimental procedure as that described in Section 2.3.1. The hydroxyl radical test using terephthalic acid (0.5 mM) was performed by employing an LS50B spectrophotometer (Perkin Elmer Ltd.) equipped with a Xenon discharge lamp and an R928 photomultiplier. The obtained solution was measured at an excitation wavelength of 315 nm.

2.3.2. Action spectra analysis (monochromatic irradiation)

Action spectral measurements were performed for selected Ln(ndc)-modified TiO_2 photocatalysts. Experiments were performed in a reactor at initial phenol and photocatalyst concentrations of 0.21 mM and 10 g/L, respectively. The reaction mixture was irradiated at monochromatic wavelengths for 90, 180, or 360 min (Table S1) using a tunable monochromatic light source (1000 W Xe lamp LSH602 and LOT-Quantum Design monochromator MSW306). The different exposure times for individual monochromatic wavelengths resulted from characteristic Ln^{3+} absorption bands, which were assigned to the transitions from the Ln^{3+} ground state, and were responsible for the UC process. The light intensity was measured using an optical power meter (ILT2400, International Light Technologies). During the experiments, the reactor was maintained at ambient temperature and the reaction mixture was continuously stirred. The samples (~0.1 mL) for HPLC analysis were collected at 30 min intervals. The apparent quantum efficiency (AQE) as a function of wavelength was calculated based on the ratio of the rate of electron consumption (rate of benzoquinone generation) to the flux of incident photons, assuming that two photons were required according to the reaction stoichiometry.

3. Results and discussion

Hybrid materials based on TiO_2 and LnOFs were synthesised using a three-step process (Fig. 1a). The synthesis started from the preparation of TiO_2 spheres by the direct precipitation of titanium isopropoxide [21]. TiO_2 was functionalised with a carboxylic group monolayer using the silane coupling agent APTES and succinic anhydride [22]. Subsequently, a solvothermal reaction allowed the epitaxial Ln(ndc) MOF growth of the surface-anchored TiO_2 [23]. In general, the formation of Ln(ndc) MOFs includes two steps: (1) dissociation of carboxylic acids (protonated ligands) and (2) crystallisation of Ln(ndc) including nucleation and growth. Based on the literature data and prior studies in our research group [24,25], it is observed that the strategy for the fabrication of MOF/heterointerfaces is advantageous compared to the fast one-pot solvothermal reaction to achieve uniform thin film growth because it affords selective and directional growth with reduced number of defects at the interfacing sites [24,25]. The description and physicochemical characterization data of the as-prepared photocatalysts are summarised in Table 1.

3.1. Morphology

The morphological and structural features of the as-prepared Ln(ndc)/TiO_2 composites were investigated by SEM and TEM, and the results are shown in Figs. 1b–g, S1, and Figs. 2, S2, respectively. SEM images show that pristine TiO_2 has uniform spherical structure with a size distribution of 400–650 nm (Fig. S1d). The surface of TiO_2 is smooth, without noticeable granular features. Following carboxyl functionalization, the surface is roughened because of the modification. After in situ growth *via* solvothermal treatment, a layer of Ln(ndc) polyhedrons grows on the TiO_2 surface; the surface of the nanosphere becomes more rough and wrinkled (flower-like spheres are formed) after loading, which indicates that Ln(ndc) is successfully coated on the surfaces of the TiO_2 spheres. For the composites containing the highest amount of Ln(ndc) (50 wt.%), Ln(ndc) nanostructures are not well-connected to the TiO_2 spheres and Ln(ndc) shows aggregation. Furthermore, pristine LnOF has a spherical polyhedron-like structure, which is similar to the surface of Ln(ndc)/TiO_2. The average diameter of Ln(ndc) is 100–200 nm. TEM observations of pristine and modified TiO_2, as well as Ln(ndc)/TiO_2, confirm that the modification of the substrate significantly develops its external surface, and the 15–25% Ln(ndc) addition causes the presence of a flake external phase, which with 50% of Ln(ndc) transforms into the structure surrounding the entire substrate (Fig. S2). Electron diffraction pattern (Fig. 2a) revealed the presence of an additional diffraction ring in the approximately 8 Å interplanar distance. Dark-field imaging in that region (Fig. 2e, f) showed that apart from the presence of the new phase within the external flake-like structures, the presence of the phase in the outer surfaces of the substrate can be also observed. Imaging at higher magnifications shows an amorphous-like structure of the flakes, with a nanometric-size Ln(ndc) phase precipitates (Fig. 2d). As expected, the proposed LnOFs can be evenly decorated on the negatively charged TiO_2-COOH surface; moreover, the formation of nanocomposites is not affected by the metal type in LnOFs [26,27]. Yuan et al. [28] reported that the positively charged UC nanoparticles (UCNPs, $NaYF_4$:Yb/Er) could be uniformly distributed over all negatively charged MOFs such as UiO-66, MOF-801, and PCN-223. In contrast to the positively charged MOF crystals including ZIF-8, UiO-67, and MIL-101, a mixture of MOF crystals and UCNPs without the formation of nanocomposites was obtained.

3.2. Crystal structure and surface composition

The pXRD data of hybrid materials show multiple diffraction reflections in the range of 2Θ = 5–24° and 2Θ = 24–70°, corresponding to

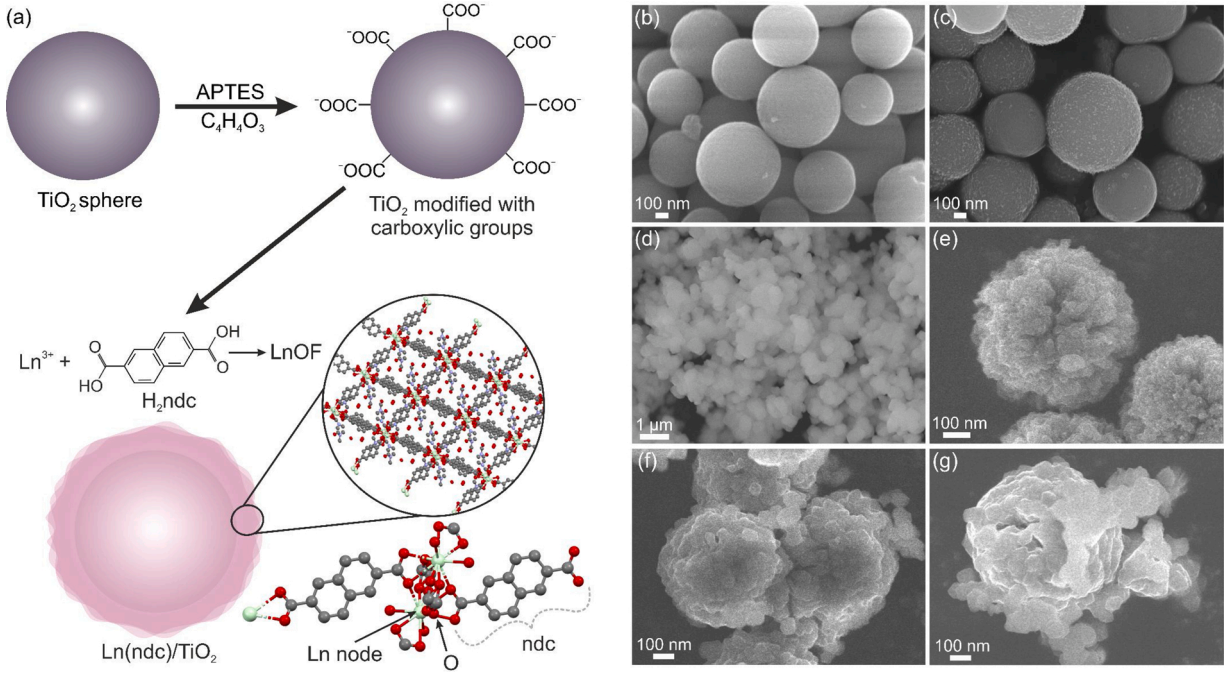

Fig. 1. (a) Schematic of the structure of Ln(ndc) MOFs grown around TiO_2 spheres. Scanning electron microscopy images of pristine (b) and carboxyl-functionalised (c) TiO_2, pristine Ln(ndc) MOFs (d), and Ln(ndc)/TiO_2 (15, 25, and 50 wt.%) composites (e–g). LnOF crystal structure proposed using the Mercury software, based on literature reports [26].

Table 1
Description and physicochemical characterization of photocatalysts.

Sample	Ln^{3+} type	Linker type	LnOF content (wt.%)	BET surface area (m^2/g)	Total pore volume (cm^3/g)	XRD lattice parameters for TiO_2 (anatase)		Crystallite volume D (Å)
						a = b (Å)	C (Å)	
TiO_2	None	None	0	67.0	0.031	3.7854 (5)	9.492 (1)	100
TiO_2_COO^-	None	None	0	56.5	0.028	3.7855 (5)	9.492 (1)	110
15%Nd(ndc)/ TiO_2	Nd	2,6-naphthalene dicarboxylic acid	15	47.2	0.022	3.784(1)	9.486 (2)	90
25%Nd(ndc)/ TiO_2	Nd		25	33.0	0.016	3.785(1)	9.488 (3)	90
50%Nd(ndc)/ TiO_2	Nd		50	15.6	0.008	3.789(2)	9.474 (7)	90
15%Er(ndc)/ TiO_2	Er		15	36.1	0.018	3.788(1)	9.487 (3)	100
25%Er(ndc)/ TiO_2	Er		25	33.4	0.016	3.787(2)	9.491 (6)	100
50%Er(ndc)/ TiO_2	Er		50	27.9	0.016	3.785(1)	9.491 (3)	90
15%Ho(ndc)/ TiO_2	Ho		15	36.9	0.018	3.7871 (8)	9.488 (2)	90
25%Ho(ndc)/ TiO_2	Ho		25	23.9	0.012	3.788(1)	9.491 (3)	90
50%Ho(ndc)/ TiO_2	Ho		50	9,8	0.005	3.785(4)	9.491 (8)	100
15%Tm(ndc)/ TiO_2	Tm		15	33.3	0.016	3.787(2)	9.495 (3)	100
25%Tm(ndc)/ TiO_2	Tm		25	303	0.015	3.789(2)	9.499 (5)	100
50%Tm(ndc)/ TiO_2	Tm		50	21.5	0.010	3.787(3)	9.492 (8)	100
Nd(ndc) MOF	Nd		100	7.6	0.004	–	–	–
Er(ndc) MOF	Er		100	2.8	0.001	–	–	–
Ho(ndc) MOF	Ho		100	8.3	0.004	–	–	–
Tm(ndc) MOF	Tm		100	3.2	0.002	–	–	–

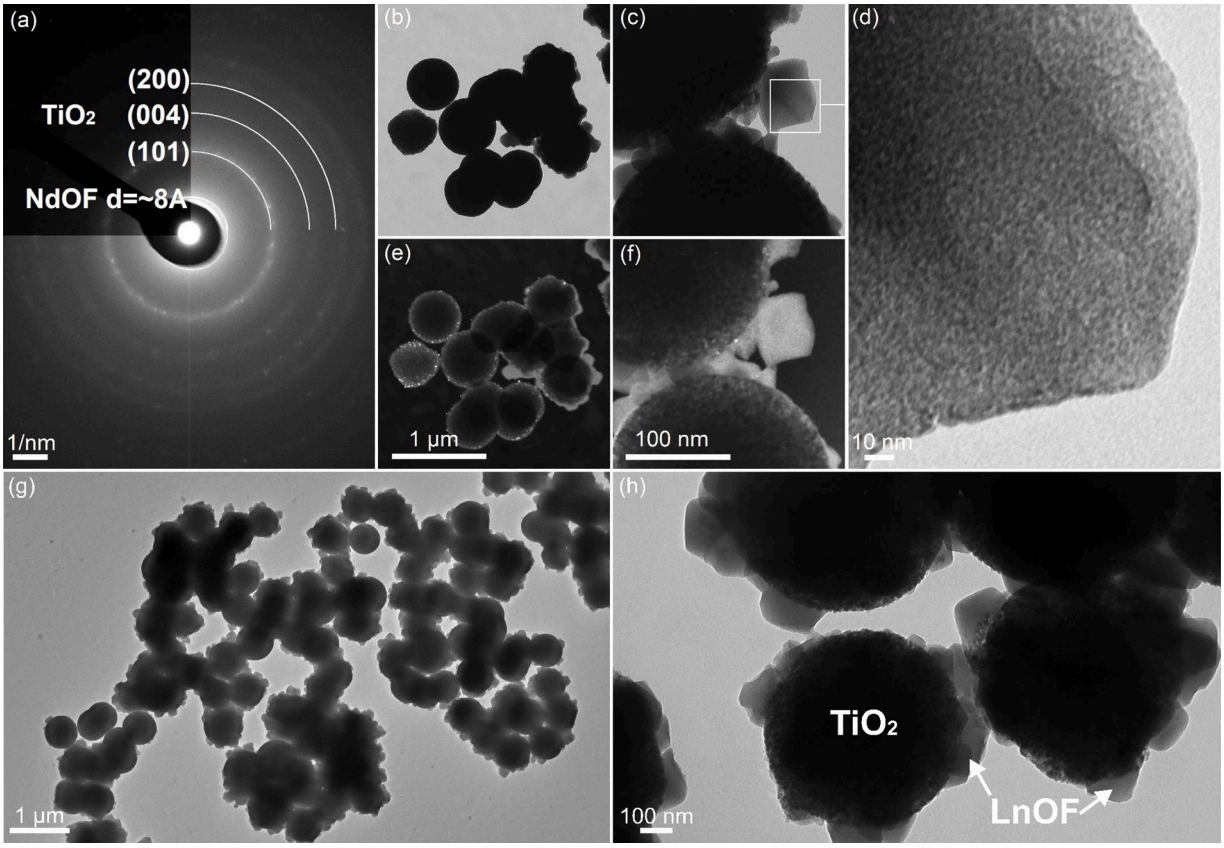

Fig. 2. TEM observations of Nd(ndc)/TiO_2: (a) selected-area electron diffraction pattern, (b, c, g, h) bright-field and (e, f) dark-field images of NdOF, (d) magnified bright-field image.

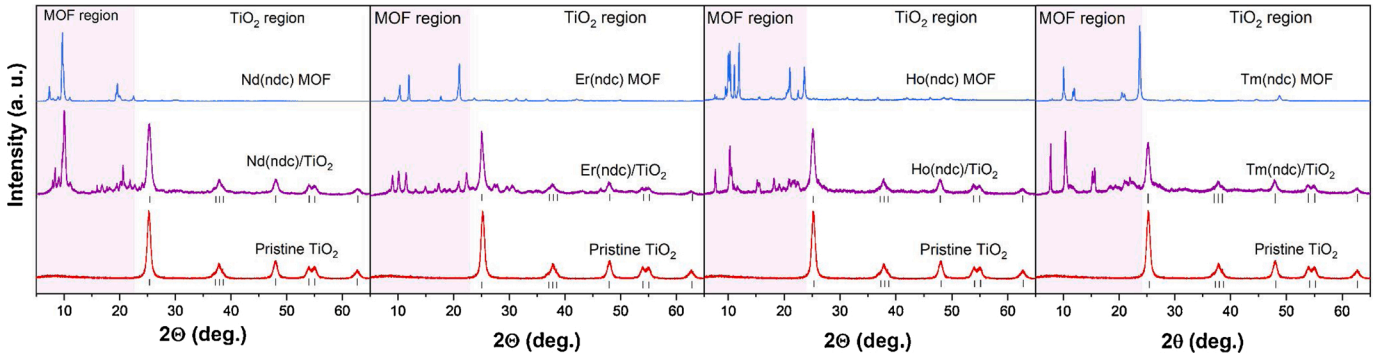

Fig. 3. Powder X-ray diffraction patterns of Ln(ndc) MOFs, Ln(ndc)/TiO_2 composites, and pristine TiO_2 (l – TiO_2 anatase).

the crystalline lattice of the Ln(ndc) MOFs and TiO_2 template, respectively (Fig. 3). For pristine TiO_2, all the diffraction reflections can be assigned to the anatase form of TiO_2 (JCPDS no. 21-1272), and the estimated lattice constants are a = b = 3.7854(5) Å and c = 9.492(1) Å, with α = β = γ = 90° [29]. For the TiO_2 phase, the crystallite size D was calculated using the Scherrer equation and was between 90 Å and 100 Å for all the analysed samples (Table 1). The estimated values of the lattice constants and crystallite sizes in the anatase phase remain statistically unchanged. The diffraction patterns of the as-synthesized Ln(ndc) MOFs indicate that all investigated complexes form crystalline powders, and sharp peaks characteristic of the ordered structures can be observed. The pXRD patterns are consistent with those reported previously in the literature [30–32]. TiO_2 crystallinity is well preserved during Ln(ndc) MOF formation; all indices corresponding to the anatase phase are observed in the pXRD patterns of the hybrid materials with relative intensities of the peaks remaining the same as those for pristine TiO_2. Moreover, this observation confirms that the dissolution and growth processes maintain the crystalline structure of the parent TiO_2 during Ln (ndc) MOF formation.

The characteristic vibration bands of the pristine as well as carboxyl-functionalised TiO_2 and Ln(ndc) MOFs formed around TiO_2 were identified using FTIR spectroscopy (Figs. 4 and S3), and 2,6-ndc was used as the reference. The FTIR spectrum of pristine TiO_2 shows absorption peaks at approximately 1637 cm^{-1}, corresponding to the deformative vibration of Ti-OH stretching mode, and a band below 850 cm^{-1}, which is correlated to the Ti–O–Ti bond in TiO_2 [33]. After carboxyl functionalisation, the appearance of the characteristic –CO–NH– peak at 1444 cm^{-1} indicates the successful modification of TiO_2 with the carboxyl groups, which are formed using APTES [22]. Moreover, the presence of a characteristic band at 1419 cm^{-1} is observed, which is

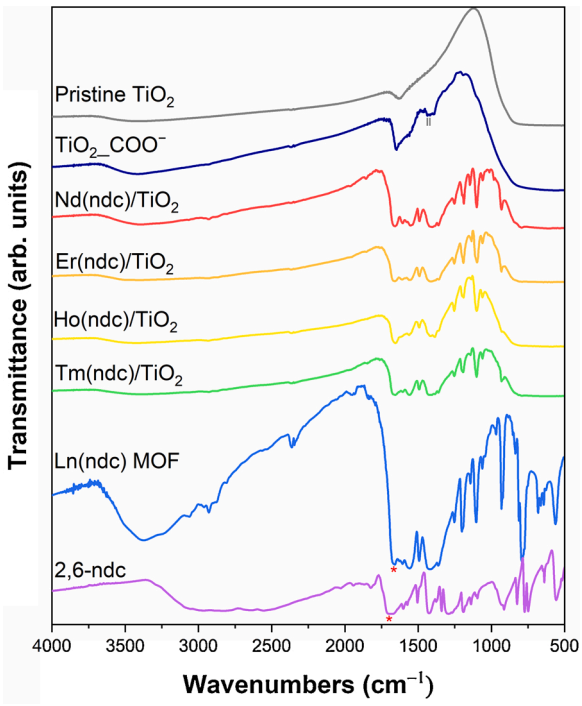

Fig. 4. Fourier transform infrared spectra of pristine TiO_2, carboxyl-functionalised TiO_2, Ln(ndc)/TiO_2 composites, and 2,6-ndc linker (new peaks after carboxyl functionalisation: grey lines; deprotonation of 2,6-ndc: red stars).

assigned to the carboxylate groups (–COO–) anchored to the TiO_2 surface [33,34]. Finally, the appearance of new bands at 929–1668 cm^{-1} in the FTIR spectrum confirms the successful Ln(ndc) MOF coating of the TiO_2 spheres. The as-prepared Ln(ndc)/TiO_2 hybrid materials show vibration bands at approximately 1664 cm^{-1} (C = O vibration between DMF and Ln in the frameworks), 1658 cm^{-1} (Ln vibration in the frameworks), 1187 cm^{-1} (stretching C═C vibration of the aromatic group), 1101 cm^{-1} (stretching vibration of Csp^2-N for DMF compounds in the frameworks), 1060 cm^{-1} (C═O stretching vibration in the frameworks), and 929 cm^{-1} (bending vibration of Csp^2-H of substituted naphthalene) [35,36]. Furthermore, the Ln(ndc)/TiO_2 data show bands at approximately 1565 cm^{-1} and 1425 cm^{-1}, which are assigned to the antisymmetric and symmetric stretching vibration modes of the carboxyl group, respectively. According to the literature reports [37,38], the type of interaction between the carboxylate head and lanthanide metal ions can be confirmed by the wavenumber separation of these bands: the largest (200–320 cm^{-1}) corresponds to monodentate interaction, medium (140–190 cm^{-1}) to bridging bidentate interaction, and the smallest (<110 cm^{-1}) to chelate interaction [37,38]. Herein, the distance is ~140 cm^{-1}, which is attributed to bidentate bridging; thus, the formation of the complex structure between carboxylate-terminated TiO_2 and Ln(ndc) MOFs is probably achieved by Ln metal ions, which easily coordinate to 2,6-ndc for the growth of LnOFs. The FTIR spectra of the Ln(ndc) MOFs exhibit significant differences upon comparison to that of 2,6-ndc (marked with asterisk in Fig. 3). The presence of a peak at approximately 1660 cm^{-1} in conjunction with the absence of a wide absorption peak at approximately 1700 cm^{-1} confirms the deprotonation of the carboxyl groups in 2,6-ndc upon reaction with metal ions [16]. In addition, the presence of specific COO-M^+ bands at 1359 cm^{-1} confirms the successful synthesis of Ln(ndc) through the assembly of lanthanide ions and organic linkers [39,40].

The elemental composition and characteristics of the elements detected in the outermost surface areas of all the selected samples were examined by XPS. The elemental composition was determined using the HR-XPS data of the elements (Table 2). The chemical characteristics of the elements originating from pristine TiO_2 spheres (Ti, O, C), carboxylated TiO_2 spheres (Ti, O, C, N), and lanthanides (Ln = Nd, Er, Ho, Tm) coordinated within the TiO_2/lanthanide-carboxylate composites (Ln(ndc)/TiO_2) were identified based on the HR-XPS spectra shown in Fig. 5. The chemical states of Ti, O, C, N, and Ln were determined by deconvolution of the corresponding HR spectra (Fig. 5). The Ti 2p spectrum is resolved into two doublet components represented by the BEs of the Ti $2p_{3/2}$ signals at 458.6 and 457.3 eV, corresponding to Ti^{4+} and Ti^{3+}, respectively [8]. Ti^{4+} is the dominant surface state for all samples. The O 1s spectrum of pristine TiO_2 can be characterized by four states of BEs located at 529.8, 530.4, 531.1, and 531.9 eV, corresponding to TiO_2_latt, TiO_2_surf, –C═O, and –OH surface species, respectively [8,41]. However, the O 1s spectrum of the carboxylated TiO_2 spheres reveals a different chemical state composition. The main peak is observed at 529.4 eV in addition to the signals at 529.9, 530.9, and 531.8 eV; the peak at 529.4 eV can be attributed to the Ti–O bond formed by the coordination between the carbonate O atoms and TiO_2 [39,42], confirming the carboxyl functionalisation of TiO_2, while the other three peaks can be assigned to TiO_2_latt, –C═O, and surface –OH species, respectively. The successful carboxylation of TiO_2 is also confirmed by the C 1s spectra of the pristine and carboxylated TiO_2 species. The data for the former show signals at 284.8, 286.3, and 289.3

Table 2
Elemental compositions (in atomic %) of the surface layers of pristine and carboxyl-functionalised TiO_2 nanospheres and Ln(ndc)-modified TiO_2 nanosphere composites evaluated by X-ray photoelectron (XPS) spectroscopy. The corresponding composition of the pristine Ln(ndc) MOF is also presented.

Sample label	Elemental composition (atomic %.)							
	Ti	O	C	N	Nd	Er	Ho	Tm
Pristine TiO_2	25.97	63.80	10.23	–	–	–	–	–
TiO_2_COO^-	23.06	60.61	13.94	2.39	–	–	–	–
15%Nd(ndc)/TiO_2	20.91	57.66	18.55	2.54	0.34	–	–	–
25%Nd(ndc)/TiO_2	19.97	56.52	20.32	2.67	0.52	–	–	–
50%Nd(ndc)/TiO_2	7.75	35.90	53.11	2.27	0.97	–	–	–
15%Er(ndc)/TiO_2	19.23	56.08	21.61	2.69	–	0.39	–	–
25%Er(ndc)/TiO_2	16.17	49.96	30.93	2.19	–	0.75	–	–
50%Er(ndc)/TiO_2	15.50	47.77	33.97	2.00	–	0.76	–	–
15%Ho(ndc)/TiO_2	18.06	54.18	24.58	2.51	–	–	0.67	–
25%Ho(ndc)/TiO_2	16.81	50.98	29.02	2.21	–	–	0.98	–
50%Ho(ndc)/TiO_2	15.37	48.17	32.75	2.61	–	–	1.10	–
15%Tm(ndc)/TiO_2	20.99	58.48	18.10	2.14				0.29
25%Tm(ndc)/TiO_2	21.36	59.53	16.73	2.08	–	–	–	0.30
50%Tm(ndc)/TiO_2	19.35	56.04	22.21	2.02	–	–	–	0.38
Nd(ndc) MOF	–	22.05	72.81	2.87	2.27	–	–	–
Er(ndc) MOF	–	23.07	72.69	1.96	–	2.28	–	–
Ho(ndc) MOF	–	21.82	71.96	2.85	–	–	3.37	–
Tm(ndc) MOF	–	23.11	72.52	2.59	–	–	–	1.78

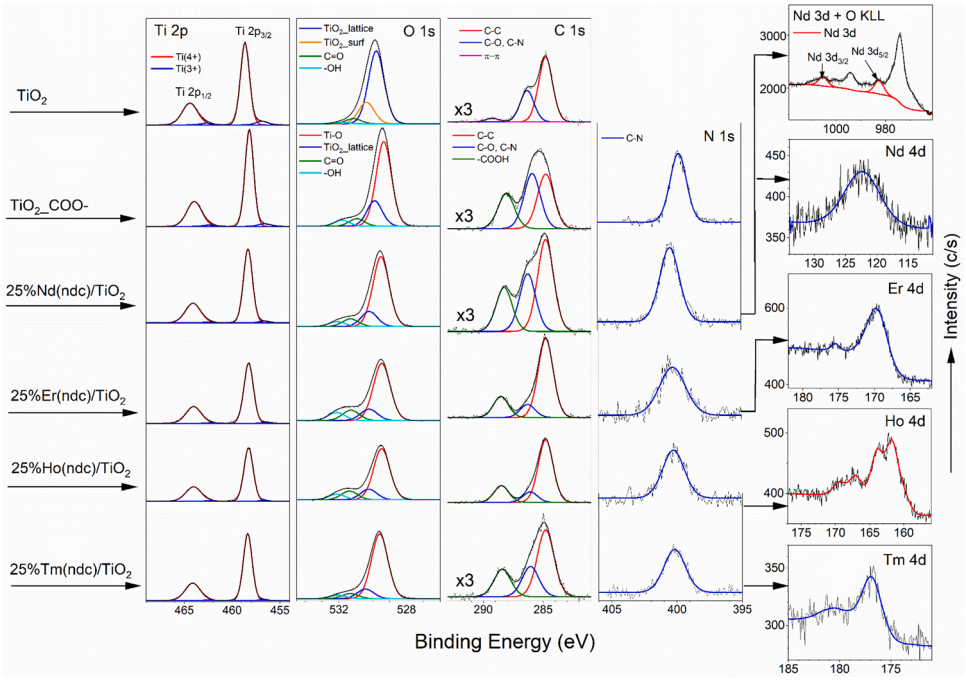

Fig. 5. High-resolution XPS data of the elements detected in pristine TiO_2, carboxyl-functionalised TiO_2 (TiO_2_COO^-), and Ln(ndc)/TiO_2 (25 wt.%) nanocomposites.

eV, which can be attributed to C—C, C—O, and π-π bonds, respectively, whereas those for the latter exhibits peaks at 284.8, 286.0, and 288.1 eV, which are characteristic of the C—C, C—O/C—N, and —COOH bonds, respectively [8,41]. Moreover, the N1 s spectrum of carboxylated TiO_2 confirms the presence of nitrogen originating from DMF used in the carboxylation. The chemical characteristics of the surface species formed on Ln(ndc)/TiO_2 were also determined. The resulting HR-XPS data of the detected elements for the selected samples with the same nominal concentrations of Ln modifiers (25 wt.%) are shown in Fig. 5. All Ti2p, O1 s, C1 s, and N1 s deconvoluted spectra exhibit the chemical characteristics of surface species similar to those detected for carboxylated TiO_2. The successful syntheses of Nd, Er, Ho, and Tm are confirmed by the Nd3d/Nd4d, Er 4d, Ho4d, and Tm4d spectra, respectively (Fig. 5). The Nd peaks in the Nd3d spectrum (BE of Nd $3d_{5/2}$ is close to 983 eV [41]) are overlapped by the O KLL Auger signals. Therefore, the Nd 4d peak was also analysed to confirm the presence of Nd. The Nd 4d, Er 4d, Ho4d, and Tm4d peaks located at 122.3, 169.5, 163.0 and 176.8 eV (Fig. 4), indicate the presence of Nd^{3+} [8,29], Er^{3+} [29,41,43,44], Ho^{3+} [29,41,43], and Tm^{3+} [29,41,43,45] oxides, respectively. Similar spectra of Nd3d, Er4d, Ho4d, and Tm4d were recorded for pristine Ln(ndc) MOFs synthesised without TiO_2 (Fig. S4). The chemical states of other elements (O, C, and N) are similar for all Ln (ndc)MOFs (O1 s, C1 s, and N1 s deconvoluted spectra in Fig. S4). The O1 s spectra are resolved into two states, C═O and C—OH, corresponding to the peaks at 531.7 and 533.2 eV, respectively. In the C1 s spectra, the BEs of 284.8, 286.6, 288.6, and 290.3 eV can be assigned to C—C, C—O/C—N, —COOH, and π-π bonds, respectively [8,46]. The additional signal (289.5 eV) in the C 1s spectrum of the Ho(ndc)MOF sample indicates the low surface C—F contaminants [41]. The N1 s spectra are obtained owing to the DMF used in the preparation.

3.3. TGA and BET surface area measurements

The stabilities of the Ln(ndc) MOFs and TiO_2 NS composites were determined by TGA. The TGA curves, representing the mass losses of the samples as a function of temperature, were obtained for pristine and carboxyl-functionalised TiO_2, pristine Ln(ndc) MOFs, and 50 wt.% Ln (ndc)-modified TiO_2 composites (Fig. S5). The mass losses detected for the pristine and carboxyl-functionalised TiO_2 are relatively low (6.5%) below 400 °C, mainly corresponding to surface water evaporation followed by almost no changes in the structures of the materials. This observation indicates the high thermal stability of TiO_2 spheres up to 800 °C. Pristine MOFs exhibit ~25% total mass loss up to 400 °C in a two-step process (~5% and ~20% mass losses are observed below 100 °C and 200 °C, respectively), which can be attributed to both the removal of DMF and water molecules as well as the decomposition of the MOFs. In comparison, the mass changes detected for Ln(ndc)/TiO_2 nanocomposites in the preliminary stage are reflected by the vaporisation of adsorbed water or ethanol from the samples, followed by the rapid decomposition of Ln(ndc) MOFs at 150–400 °C [35]. The specific BET surface areas of pristine TiO_2, pristine Ln(ndc) MOFs, and Ln (ndc)/TiO_2 composites are listed in Table 1. The surface areas of the as-prepared samples fluctuate from 2.8–67 m^2 g^{-1} and depend on the amount of Ln(ndc) MOFs and the type of MOF in the composites. The BET surface area gradually decreases with an increase in the content of Ln(ndc) MOFs, and all hybrid composites show lower BET surface areas in comparison to that of pristine TiO_2. The relatively low BET surface areas of pristine Ln(ndc) MOFs can have a significant effect on the photocatalytic activity. However, the results are ambiguous; sharp decreases in the specific surface area and porosity may result from the applied temperature in the analysis, resulting in the collapse of the LnOF crystal structure. To obtain useful information, the MOFs should be appropriately dried and heated prior to the measurements. In some cases, such pre-treatment decreases the surface area due to framework collapse, which could often be related to the capillary forces and high surface stress in the interphase between the gas and confined molecules of the solvent [47].

3.4. Diffuse reflectance spectroscopy (DRS)

The photoresponse range of the semiconductor is an important factor that effects the performance of a photocatalyst. The DRS data of the as-prepared LnOF/TiO_2 and pristine TiO_2 were measured in the 250–850 nm range, and the results are shown in Figs. 6 and S6. The pristine TiO_2 reference sample shows absorption only in the UV region. The characteristic broad intense absorption below 390 nm is assigned to the charge

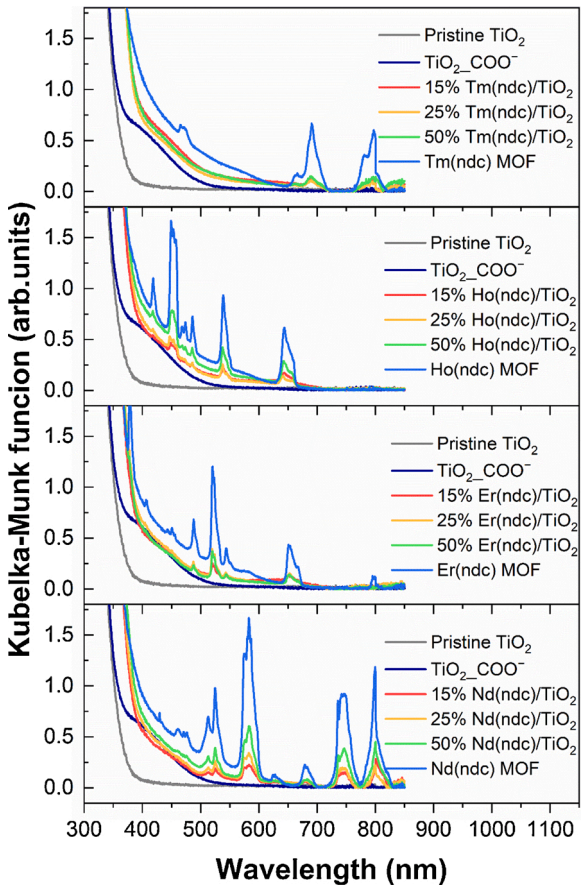

Fig. 6. Ultraviolet-visible Kubelka–Munk absorption spectra of pristine and carboxyl-functionalised TiO_2, Ln(ndc) MOFs, and Ln(ndc)/TiO_2 composites.

transfer from the O 2p valence band to the Ti 3d conduction band. All LnOF-modified TiO_2 samples show slight redshifts in their absorption edges compared to those of the unmodified sample. This commonly described phenomenon in the literature is attributed to the charge-transfer transition between the Ln^{3+} intra-4f electrons and titanium dioxide conduction/valence band (CB/VB) [48]. The optical response of LnOF in the UV region is attributed to the π–π* transitions in the organic ligands (π–π interactions of adjacent naphthalene rings), whereas the absorption band in the visible region reflects the transitions of the Nd^{3+}, Er^{3+}, Ho^{3+}, or Tm^{3+} centres. Moreover, other typical absorption bands of pristine LnOF in the visible region show some changes. The absorption bands of Nd ions are observed at wavelengths of 472, 525, 583, 680, 745, and 800 nm, originating from the $^4I_{9/2}$ ground state transition to the $^2G_{9/2} + {}^2D_{3/2}$, $^2P_{3/2}$, $^2K_{13/2} + {}^4G_{7/2} + {}^4G_{9/2}$, $^4G_{5/2} + {}^2G_{7/2}$, $^4F_{9/2}$, $^4S_{3/2} + {}^4F_{7/2}$, and $^4F_{7/2} + {}^2H_{9/2}$ excited states [8,49]. The absorption peaks at 378, 406, 450, 489, 520, 543, 652, and 796 nm indicate the presence of erbium and correspond to the transitions from the $^4I_{15/2}$ ground state to the $^4G_{11/2}$, $^2H_{9/2}$, $^4F_{5/2} + {}^4F_{3/2}$, $^4F_{7/2}$, $^2H_{11/2}$, $^4S_{3/2}$, $^4F_{9/2}$, and $^4I_{9/2}$ excited states [50–53]. The absorption peaks at 418, 450, 468, 473, 486, 538, and 643 nm, which are characteristic of holmium, can be correlated to the transitions from the $^5I_8$ ground state to the $^5G_5$, $^5G_6$, $^5G_6 + {}^5F_1$, $^5S_2 + {}^5F_4$, and $^5F_5$ excited states of holmium ions [6,54]. Thulium ions show characteristic peaks at 465, 690, 779, and 796 nm, which can be attributed to the transitions from the $^3H_6$ ground state to the $^1G_4$, $^3F_{2/3}$, and $^3H_4$ excited states of thulium [55]. In addition, the following absorption bands are observed in the visible region: 525, 583, 680, 745, and 800 nm for Nd(ndc)/TiO_2; 489, 520, 543, and 652 nm for Er(ndc)/TiO_2; 418, 450, 485, 538, and 643 nm for Ho(ndc)/TiO_2; 690 and 796 nm for Tm(ndc)/TiO_2. The intensities of the absorption bands corresponding to the presence of Ln^{3+} species increase with an increase in the concentration of Ln^{3+} species in the photocatalytic systems. The above results show that the Ln(ndc)/TiO_2 system has the capability of broadband photon harvesting from UV–vis to the near-infrared range.

3.5. Photocatalytic activity

The photocatalytic activities of pristine TiO_2, pristine LnOFs, and LnOFs/TiO_2 composites with different amounts of LnOFs were evaluated using a model phenol degradation reaction under visible light irradiation ($\lambda > 420$ nm and $\lambda > 455$ nm; Fig. 7; Table 3). Organic pollutants such as phenol and its derivatives are found in industrial wastewaters and are very toxic, non-volatile, non-biodegradable, and difficult to eliminate by conventional biological processes. Therefore, phenol is an excellent model compound for photocatalysis as a chemical treatment method [56]. The preliminary study included control tests, i.e., phenol degradation in the absence of photocatalysts and phenol degradation without visible irradiation (dark test). The measurement of photolysis under visible light irradiation without a photocatalyst showed no phenol degradation. Furthermore, adsorption experiments under dark conditions were performed to determine the effects of the MOFs on the adsorption behaviours of TiO_2 photocatalysts. The adsorption capacity of phenol in the presence of LnOF-modified TiO_2 increased slightly during the first 30 min compared to that of pristine TiO_2, and then remained almost constant for all samples. Therefore, before irradiation, the mixture containing the photocatalyst and phenol solution was stirred for 30 min in the dark to establish an adsorption–desorption equilibrium. Pristine TiO_2 showed a very low phenol degradation efficiency of only 4.6% under visible light irradiation ($\lambda > 420$ nm), and the photodegradation efficiency increased to 17.8% upon surface modification with carboxylic group. These results are consistent with the experimental observation of absorption enhancement, where the deposition of carboxylic groups on TiO_2 increases the absorption in the blue region of the visible spectrum. Additionally, no noticeable photoactivity is observed upon using pristine LnOFs (3–8%; Table 3). Nasruddin et al. [36] fabricated lanthanum–2,6-ndc MOF as a photocatalyst using the solvothermal method. No significant photocatalytic activity of the synthesised sample was reported; only 18.32% of rhodamine-b photodegraded after an exposure of 120 min to UV–vis light [36]. The photocatalytic performance of a LnOF is generally characterised by the rapid recombination of photoinduced electron–hole pairs; therefore, the integration of MOFs with other semiconductors is a promising method to enhance the efficiency of excitation generation and charge separation due to charge transfer [39,57]. The experimental results in the present study reveal that the photocatalytic activity of the hybrid material, Ln(ndc)/TiO_2, is significantly improved compared to that of pristine LnOFs or pristine TiO_2 under visible light irradiation (Table 3). The efficiency of phenol photodegradation depends on the amount of Ln(ndc) MOFs (15, 25, or 50 wt.%) and the type of lanthanide ions (Nd, Er, Ho, or Tm) in the Ln(ndc)/TiO_2 composites. The highest efficiency is achieved for the 25 wt.% Nd(ndc)-modified TiO_2 sample, affording a value of 87.5% after 60 min of exposure, which is 19 times higher than that of pristine TiO_2. Moreover, when neodymium is used as the dopant, the photodegradation efficiency increases from 82.8% for 15 wt.% of Nd(ndc) to 87.5% with an increase in the MOF concentration to 25 wt.%. The photoactivity drastically decreases to 48.1% when the composite contains 50 wt.% of Nd(ndc) MOF. The same trend is observed for Ho(ndc)- and Er(ndc)-modified TiO_2. When Tm(ndc) is used as the modifier, the photocatalytic performance under visible light irradiation decreases with an increase in the MOF content (15 > 25 > 50 wt.%). Other samples show photoactivity in the 36.9–82.8% range. The modification of TiO_2 with the highest amount of Ln(ndc) MOF (50 wt.%) results in a decline in photoactivity, which is in agreement with prior literature reports. *Zhang et al.* [58] prepared a series of TiO_2-UiO-66-NH_2 composites and demonstrated that pure UiO-66-NH_2 showed a relatively low photoactivity (7.49%), while the UV-photoconversion of toluene with TiO_2-UiO-66-NH_2 samples increased with an increase in the UiO-66-NH_2

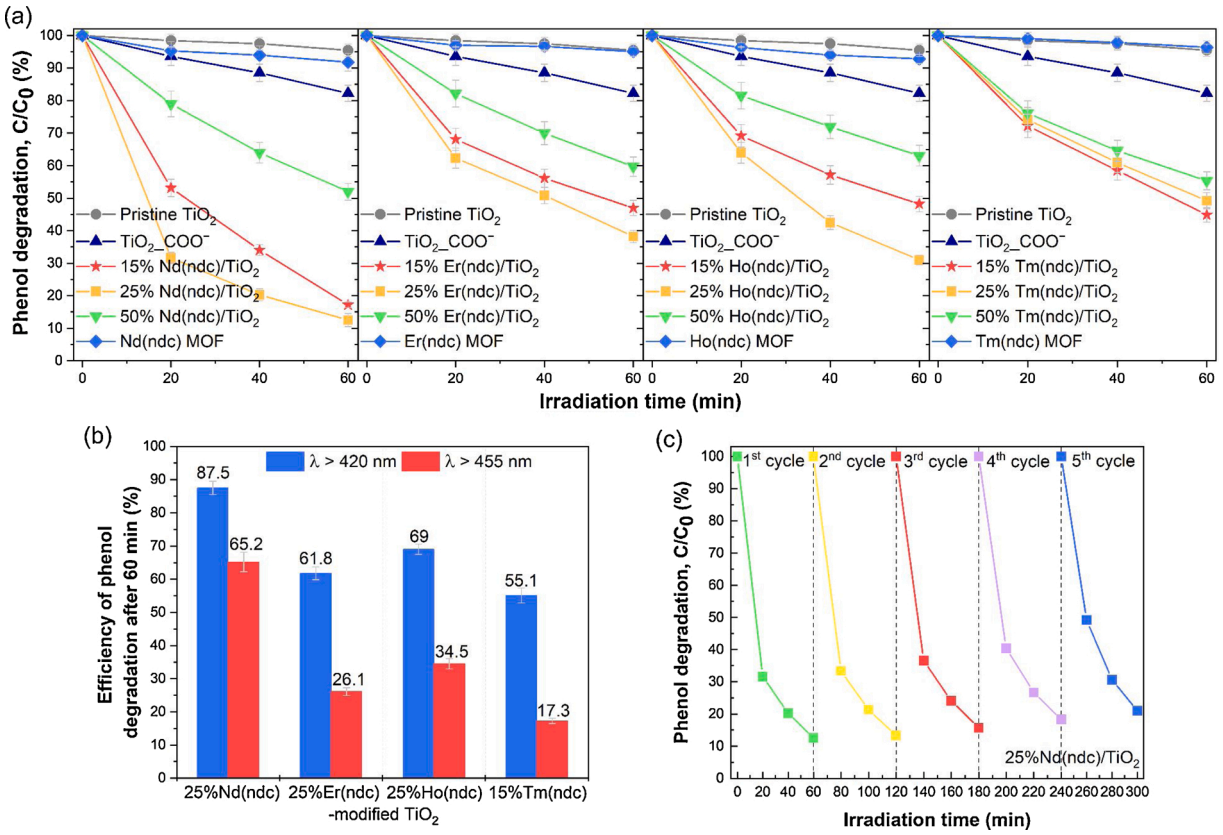

Fig. 7. (a) Efficiency of phenol degradation under visible light irradiation (λ > 420 nm) in presence of pristine and carboxyl-functionalised TiO_2, pristine Ln(ndc) MOFs, and Ln(ndc)/TiO_2 composite. (b) Efficiency of phenol degradation under irradiation at λ > 420 nm and λ > 455 nm with selected Ln(ndc)-modified TiO_2 composites. (c) Photostability during five cycles of 25%Nd(ndc)/TiO_2 usage.

content from 10 wt.% to 25 wt.%, and then decreased with further increase of the UiO-66-NH_2 content. Therefore, TiO_2 photocatalysts modified using 25 wt.% UiO-66-NH_2 exhibited the highest photocatalytic activity with 72.70% of toluene conversion after reaction for 240 min (1.64 and 9.72 times higher than those of pristine TiO_2 and UiO-66-NH_2, respectively) [58]. Crake et al. [59] synthesised NH_2-UiO-66-modified TiO_2 and observed that a nanocomposite containing a moderate amount of NH_2-UiO-66 (ca. 20 wt.%) showed the highest activity in the photocatalytic CO_2 reduction under UV–vis exposure, i.e., 1.5 times more active than pristine TiO_2 [59]. Liu et al. [60] fabricated TiO_2 modified with 20 wt.% ZIF-8 and observed that the hybrid material exhibited a higher photocatalytic reduction of Cr(VI) under UV–vis light irradiation than the pristine samples [60]. In summary, phenol photodegradation decreases in the following order: 25% Nd(ndc)/TiO_2 > 15%Nd(ndc)/TiO_2 > 25%Ho(ndc)/TiO_2 > 25%Er (ndc)/TiO_2 > 15%Tm(ndc)/TiO_2 > 25%Tm(ndc)/TiO_2 > 15%Er (ndc)/TiO_2 > 15%Ho(ndc)/TiO_2 > 50%Nd(ndc)/TiO_2 > 50% Tm (ndc)/TiO_2 > 50% Er(ndc)/TiO_2 > 50%Ho(ndc)/TiO_2.

In addition, the photocatalytic activities of the most active representatives of the Ln(ndc)/TiO_2 hybrid materials, including 25%Nd(ndc)-, 25%Ho(ndc)-, 25%Er(ndc)-, and 15%Tm(ndc)-modified TiO_2, were measured under irradiation with light of λ > 455 nm (Fig. 7b). With long irradiation wavelength, the degradation efficiency decreases to 65.1% and 26.3% in the presence of samples containing neodymium and erbium, respectively, while for holmium and thulium, the photoactivities are 34.1% and 17.5%, respectively.

The photocatalytic oxidation of phenol under visible light irradiation (λ > 420 nm) was investigated using HPLC to identify the intermediate organic compounds formed during the reaction (Table 3). Generally, the main intermediates formed in the first few minutes of irradiation include benzoquinone, hydroquinone, and catechol (Figs. S7-S10). In the presence of the four most active samples (15%Nd(ndc)-, 25%Nd(ndc)-, 25%Er(ndc)-, and 25%Ho-modified TiO_2), the highest amounts of hydroquinone in the aqueous phase are observed at the beginning of the reaction, whereas the concentration of benzoquinone decreases slowly and then increases up to 40 min of irradiation, followed by a significant decrease upon further irradiation (see supporting material for details). For the remaining samples (50%Nd(ndc)-, 15 and 50%Er(ndc)-, 15 and 50%Ho(ndc)-, as well 15, 25, and 50%Tm(ndc)-modified TiO_2), the concentrations of hydroquinone and benzoquinone increase during 60 min of irradiation. The concentrations of the intermediate products decrease slowly due to the different pathways of phenol oxidation, and the keto-enol tautomeric equilibrium between hydroquinone and benzoquinone retards the rate of phenol photomineralization [61]. Furthermore, the catechol concentration increases with an increase in the irradiation time for selected samples, and the highest amount is observed for 25%Nd(ndc)/TiO_2 (Fig. 9a). The formation of catechol is not detected in the suspension after phenol degradation with the Tm (ndc)-modified TiO_2 photocatalytic systems. Both the amounts and types of intermediates formed during phenol degradation depend on the kinetics as well as the type of reactive species generated on the photocatalyst surface [62].

The most active sample (25%Nd(ndc)/TiO_2) shows a modest decrease in the photocatalytic activity (~8%) over five consecutive runs with a total length of 300 min (Fig. 7c). The slight loss of the photocatalytic activity is often described in the literature and could be explained by adsorption of pollutants on the reactive sites of the photocatalyst [63,64] or by changing of the photocatalyst structure/surface composition [65,66]. In the case of Ln(ndc)/TiO_2 composite, TiO_2 is expected to remain unchanged, while metal-organic framework could be transformed by radiation or active species generated during reaction. To elucidate the evolution of chemical properties of the most active 25%Nd

Table 3
Photocatalytic activities of pristine and carboxyl-functionalised TiO_2, pristine Ln(ndc) MOFs, and Ln(ndc)/TiO_2 composite photocatalysts under visible light irradiation.

Sample	Efficiency of phenol adsorption after 30 min in dark (%)	Phenol degradation rate at $\lambda > 420$ nm (umol·dm^{-3}·h^{-1})	Efficiency of phenol degradation at $\lambda > 420$ nm after 60 min (%)	Amounts of generated intermediates after 60 min of visible light irradiation ($\lambda > 420$ nm) (mg/L)		
				Catechol	Hydroquinone	Benzoquinone
Pristine TiO_2	1.9	9.7	4.6	–	–	–
TiO_2_COO^-	3.1	37.8	17.8	–	0.19	0.07
15%Nd(ndc)/TiO_2	8.5	175.9	82.8	0.95	1.62	1.06
25%Nd(ndc)/TiO_2	9.1	185.9	87.5	1.11	1.73	1.16
50%Nd(ndc)/TiO_2	16.2	102.0	48.1	0.52	0.79	0.86
15%Er(ndc)/TiO_2	3.9	112.7	53.0	0.83	1.21	0.70
25%Er(ndc)/TiO_2	11.7	131.3	61.7	0.86	1.27	0.76
50%Er(ndc)/TiO_2	18.6	85.7	40.3	0.38	0.41	0.53
15%Ho(ndc)/TiO_2	6.0	110.0	51.8	0.79	1.13	0.89
25%Ho(ndc)/TiO_2	9.2	146.7	69.0	0.82	1.28	0.77
50%Ho(ndc)/TiO_2	12.1	78.5	36.9	0.37	0.89	0.60
15%Tm(ndc)/TiO_2	6.4	117.2	55.1	–	1.00	0.77
25%Tm(ndc)/TiO_2	5.7	114.3	50.8	–	0.78	0.60
50%Tm(ndc)/TiO_2	11.4	94.9	44.7	–	0.52	0.40
Nd(ndc) MOF	7.6	17.5	8.2	–	–	–
Er(ndc) MOF	5.5	10.6	5.0	–	–	–
Ho(ndc) MOF	5.9	15.3	7.2	–	–	–
Tm(ndc) MOF	4.6	7.6	3.6	–	–	–

– below limit of detection.

(ndc)/TiO_2 composite under visible light irradiation we characterized the HR XPS spectra taken before and after usage of this composite in three and five cycles of photocatalytic reaction (Fig. S11 and Table S2). The increase of surface amount of carbon accompanied by decrease of titanium, oxygen and nitrogen composition is clearly observed after successive irradiation cycles. The increase of C/Ti and C/N ratios after subsequent cycles confirm the growing adsorption of carbon-like products of phenol degradation (Table S2). However it is interesting to note the relative increase of Nd atom concentration within the surface layer of irradiated 25%Nd(ndc)/TiO_2 to compare with primary material taken before irradiation (compare the corresponding Nd/C and Nd/Ti ratios in Table S2). This can indicate partial rearrangement of 25%Nd(ndc)/TiO_2 photocatalyst during prolonged time of visible light irradiation. The structure of the sample prior to and after the photocatalytic reaction was also examined by XRD (Fig. S12), and it was illustrated that no noticeable difference was found from the comparison of fresh and after 3-cycle used 25% Nd(ndc)/TiO_2 sample. However, after additional 2-cycles, the strongest Nd(ndc) MOF reflection at $2\Theta = \sim 10$ deg. (d =8.8 Å) vanishes and the unknown phase with the largest d-spacing d =11.9 Å appears. This shows that Ln(ndc)/TiO_2 can serve as a novel, quite long-lasting, and efficient photocatalytic composite material for the photodegradation of organic pollutants under visible light irradiation.

3.6. Elucidation of the mechanism

The photocatalytic process typically consists of three steps: (1) absorption of photons with a specific energy, (2) generation, separation, migration, or recombination of photogenerated electron–hole pairs, and (3) redox reactions on the photocatalyst surface. To determine the possible mechanism of the photocatalytic degradation of phenol, multistage tests were performed. The UC process involves the excitation of a material with low-energy photons, which stimulates the emission of high-energy photons.

The photocatalytic reactions performed in the presence of LnOFs may exhibit two UC mechanisms (Fig. S13). The first mechanism involves a simple single-centre UC process, namely, a mechanism consisting of ground-state absorption and excited-state absorption (GSA/ESA), in which two photons are sequentially absorbed through GSA by an ion responsible for UC, known as an activator. Consequently, ESA occurs *via* a real intermediate energy level, and the same centre then emits UC luminescence [67]. The Nd^{3+}, Er^{3+}, Ho^{3+}, and Tm^{3+} activators used in this study are characterised by ladder-like arranged energy levels, which favour the GSA/ESA process [68]. The second likely mechanism involved in the UC process of LnOF is ground-state absorption followed by energy transfer UC (GSA/ETU). It involves a pair of identical ions in close proximity, called the activator–activator pair, where the intermediate states of two identical centres are excited by GSA, followed by the excitation of one of the centres to a higher energy level *via* energy transfer (ET) [67]. To fully establish the exact visible range in which the obtained Ln(ndc)-modified titania photocatalysts were excited, oxidised phenol was investigated as a function of the excitation wavelength. Based on the AQE (action spectra) measurements, it is possible to determine the aspect of light absorbed by the photocatalyst that is involved in the photocatalytic reactions. The action spectral analysis of phenol oxidation with 25%Nd(ndc)-TiO_2 is shown in Fig. 8a, whereas the results for 25%Ho(ndc), 25%Er(ndc), and 15%Tm (ndc)-modified TiO_2 are shown in Figs. S14-S16. For comparison, the wavelength-dependent AQEs determined for pristine TiO_2 are also shown. All tested Ln(ndc)/TiO_2 photocatalysts are highly photoactive in the visible region at 400–500 nm, whereas pristine TiO_2 is active only at 400−440 nm. The AQE values calculated for the composite materials are significantly improved compared to that of the pristine sample. In

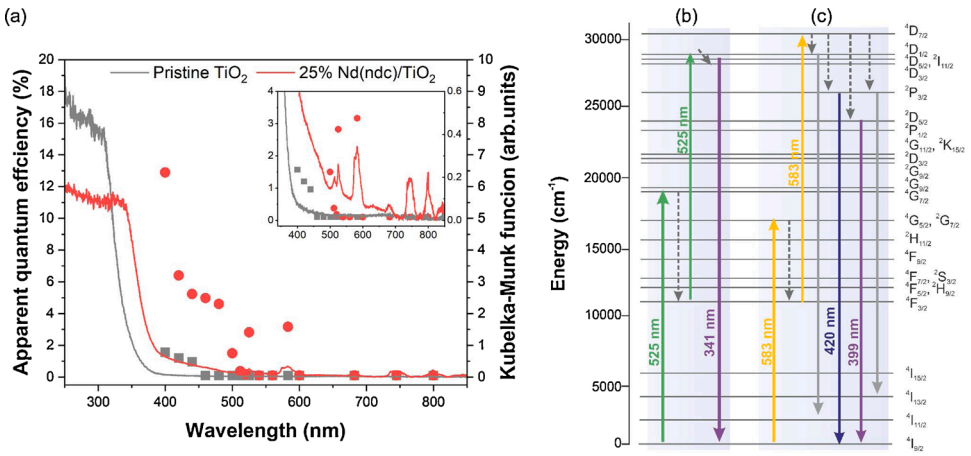

Fig. 8. (a) Action spectral analysis of phenol oxidation with 25%Nd(ndc)/TiO_2 (apparent quantum efficiency: squares and circles; photoabsorption presented as K–M function: lines). Simplified energy level diagrams of Nd^{3+} and excitation path for the up-conversion emission of ultraviolet light under (b) 525 nm and (c) 583 nm excitation.

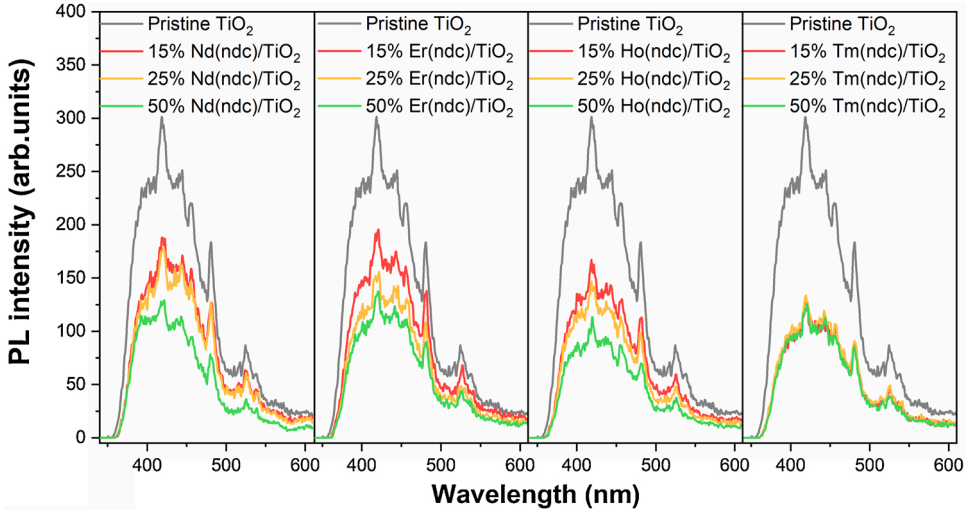

Fig. 9. Photoluminescence spectra of pristine TiO_2 and Ln(ndc)/TiO_2 composites.

addition, the composites were excited with the photon energy corresponding to the absorption bands (Fig. 6 and Table S1), which were assigned to the transitions from the Ln^{3+} ground state, and were thus responsible for the UC process. Of all the samples, the MOF containing the Nd^{3+} species exhibits the most interesting UC properties (Fig. 8a). The AQEs at 525 and 583 nm are 2.8% and 3.2%, respectively. The UC emission mechanism is explained using the energy level diagram of Nd^{3+}, as shown in Fig. 8b and c. Upon exposure at 525 nm, the Nd^{3+} species are excited from the $^4I_{9/2}$ ground state to the $^4G_{7/2}$ excited state, which subsequently relax non-radiatively to the metastable $^4F_{3/2}$ state. Thereafter, this low-lifetime (~0.4 ms) excited state absorbs a second photon promoting Nd^{3+} to the highest $^2D_{7/2}$ level, which immediately relaxes to the $^4D_{3/2}$ level. Eventually, its decays radiatively to the $^4I_{9/2}$ ground multiplets, causing emissions at 340 nm [69]. In turn, the UC Nd^{3+} emission upon excitation at 583 nm corresponds to the $^4I_{9/2} \rightarrow {}^4G_{5/2}$ transition, which is a hypersensitive band and satisfies the selection rules of $\Delta J = \pm 2$, $\Delta L = \pm 2$, and $\Delta S = \pm 0$. Specifically, this process starts from the $^4I_{9/2}$ ground state to the $^4G_{5/2}$ excited state, followed by fast photon deexcitation, populating the metastable state $^4F_{3/2}$. The excited ions jump from this level to the highest $^4D_{5/2}$ level by absorbing a second photon. Furthermore, emission from Nd^{3+} occurs when it decays non-radiatively to the corresponding lower energy levels ($^4D_{3/2} \rightarrow {}^4I_{11/2}$, $^2P_{3/2} \rightarrow {}^4I_{13/2}$) as well as upon relaxation to the $^2P_{3/2}$ and $^2D_{5/2}$ levels, and finally radiative decay to the $^4I_{9/2}$ ground multiplets, resulting in UC emissions at 399 and 420 nm [20,69]. As the 2,6-ndc ligand shows no absorption at 525 and 583 nm in the absorption spectrum (Fig. S17), the excitation at 525 and 583 nm should correspond to the $^4I_{9/2} \rightarrow {}^4G_{7/2}$ and $^4I_{9/2} \rightarrow {}^4G_{5/2}$ transitions of Nd^{3+}, respectively. Moreover, ETU involves the interaction of two excited Nd^{3+} species in the $^4F_{3/2}$ metastable state. According to the literature data [20,30], it can be concluded that a relatively short distance (4.033 Å) between the dinuclear Nd^{3+} species bridged by the carboxylate O atom allows a facile energy transfer between two optically active Nd^{3+} species, resulting in an efficient UC through the GSA/ETU process. However, the GSA/ESA mechanism may coexist in the UC process [20,30]. The action spectral analysis of phenol oxidation with 25%Ho(ndc)-, 25%Er(ndc)-, and 15% Tm(ndc)-modified TiO_2 was performed under specific monochromatic wavelengths (Figs. S14-S16). The AQE is only observed at short wavelengths, where the absorption bands of Er^{3+} and Tm^{3+} do not cause the excitation of the composite samples. In addition, for 25%Ho(ndc)/TiO_2, a response is recorded only at 450 nm (AQE = 1.2%), while the other excited states of holmium do not participate in TiO_2 activation. Simultaneously, a response in the visible region is observed at 400, 420, 440, 460, and 480 nm, i.e., in the regions without Ho^{3+}, Er^{3+}, or Tm^{3+} absorption bands. It is speculated that the UC processes occur *via* IR-to-Vis or Vis-to-Vis energy transfer with emission wavelengths of > 480 nm;

consequently, the LnOFs cannot excite TiO_2. Therefore, it can be deduced that the UC process is not responsible for the activities of 25% Ho(ndc)-, 25%Er(ndc)-, and 15%Tm(ndc)-modified TiO_2 photocatalysts in the visible region, and the compound containing Nd^{3+} shows UC.

To further elucidate the mechanism of Ln(ndc)/TiO_2 photocatalysts, the PL spectra (Fig. 9) were obtained to characterise the electron–hole recombination behaviour. Under an excitation wavelength of 315 nm, pristine TiO_2 shows a strong and broad emission at 350–600 nm, which suggests a high recombination rate of the photogenerated charge carriers. Based on the shapes of the spectra, the presence of Ln(ndc) MOF does not result in new PL phenomena. Moreover, the Ln(ndc)/TiO_2 composite samples show lesser PL emissions than those of pristine TiO_2, which may be due to the efficient charge dissociation and migration between the formed Ln(ndc) MOFs and TiO_2 heterojunction. The recombination rate depends on the amount of Ln(ndc) species on the TiO_2 surface and follows the order 15 < 25 < 50 wt.% Ln(ndc). However, modification with a high amount of MOF can result in LnOFs acting as the recombination centres. Composites containing 50 wt.% of LnOFs exhibit lower photocatalytic activities than those with 15 and 25 wt.% Ln(ndc)/TiO_2. According to the literature [70], exceeding the optimum modifier limit can afford an extremely narrow space charge layer such that the light penetration depth exceeds the width of this space charge layer; consequently, the recombination rate increases because of a lack of driving force to separate them [70]. The obtained results demonstrate that the Ln(ndc)/TiO_2 composites are characterised by high efficiencies of generation, separation, and transfer of photoinduced electron–hole pairs, which lead to high lifetimes of the charge carrier species and increase in the photocatalytic performance.

To identify and determine the major reactive species involved in the photocatalytic degradation of phenol under visible light irradiation (λ > 420 nm), two types of tests were performed, i.e., hydroxyl radical generation using terephthalic acid (TPA), and active species trapping experiment in the presence of different types of scavengers. The fluorescence (FL) spectra show the emission of 2-hydroxyterephthalic acid, which is produced by the reaction of TPA with hydroxyl radicals. The FL intensity of 2-hydroxyterephthalic acid is proportional to the amount of hydroxyl radicals generated at the photocatalyst surface. As shown in Fig. 10a, the presence of LnOFs results in increases in the intensities of the peaks compared to those of pristine TiO_2. Generally, in the presence of Er/Ho/Tm-(ndc)/TiO_2, the concentration of $^{\bullet}OH$ species increases continuously; however, the FL intensity is relatively low in comparison to that reported in the literature data [71], suggesting that $^{\bullet}OH$ species play a secondary role in phenol oxidation under visible light irradiation. Nd(ndc)-modified TiO_2 exhibits a significantly higher capability to generate $^{\bullet}OH$ species, thereby affording better photocatalytic activity in comparison to those of other modified samples. In addition, compared to the prior reports, the FL intensity and amount of $^{\bullet}OH$ generated with Nd (ndc)/TiO_2 under visible light irradiation are comparable to those produced in the UV–vis/TiO_2 system [8,72]. The obtained results, including no correlation between the amount of $^{\bullet}OH$ species and photoactivity, indicate that other reactive species are also involved in phenol degradation by the Ln(ndc)-modified TiO_2 samples. Active-species trapping experiments were conducted, providing a significant amount of information regarding various pathways by which the reactive species were photogenerated, leading to the degradation of phenol under visible light irradiation. In this study, silver nitrate, ammonium oxalate benzoquinone, and *tert*-butanol were used to quench the electrons, holes, and superoxide and hydroxyl radicals. A decrease in degradation efficiency indicates the formation of suitable active species. The effects of the addition of different scavengers on the degradation efficiency of phenol by 25%Nd(ndc)-, 25%Ho(ndc)-, 25%Er(ndc)-, and 15%Tm(ndc)-modified TiO_2 are shown in Fig. 10b. The results indicate the various pathways by which the reactive species are generated using different Ln (ndc)/TiO_2 photocatalytic systems. It is clearly observed that superoxide radicals are the main active species produced by the Ln(ndc)/TiO_2 composites. Nevertheless, photogenerated electrons also play an important role in the photocatalytic reaction of 25%Ho(ndc)-, 25%Er (ndc)-, and 15%Tm(ndc)-modified TiO_2, while 25%Nd(ndc)-TiO_2 photodegrades phenol *via* electrons and $^{\bullet}OH$ radicals.

The band gap energies (Eg) value of TiO_2 and Ln(ndc) MOF were determined by UV–vis absorption spectroscopy by using the relation Eg = 1240/ λ (Fig. S18), and were estimated to ~3.2 and ~2.9 eV, respectively. According to the Mulliken electronegativity theory formulas, the position of the levels of the VB and CB of TiO_2 were calculated to 2.90 and -0.29 eV relative to the NHE level, respectively [73]. Commonly, the highest-occupied molecular orbital (HOMO) energy level of MOF is regarded as that of the organic linker, while redox potential energy of the metal-oxo cluster is regarded as the lowest-occupied molecular orbital (LUMO) energy level of the MOF [74]. Literature data on solid-state cyclic voltammetry revealed that the 2,6-ndc linker has a redox potential at 0.47 V vs. Ag/AgCl (i.e. 0.67 V vs. NHE) [75]. Thus is can be estimated that the LUMO of Ln-MOF is -2.23 V vs. NHE. The possible mechanism for the photocatalytic processes over Ln(ndc)/TiO_2 materials was proposed based on energy levels (Fig. 11a) and charge carrier migration, which is discussed in detail in the next paragraph.

When the molecular species are adsorbed onto the surface of a semiconductor, the electronic structures of both counterparts are perturbed. This process involves some electronic coupling. Based on the above experimental results (supported by action spectral analysis, photoluminescence spectra, species trapping experiments), the enhanced photocatalytic activities of Ln(ndc)/TiO_2 materials under visible light irradiation can be described based on two diverse mechanisms, that is, the formation of a charge-transfer complex between the n-type TiO_2 semiconductor and LnOF, and up-conversion mechanisms (Fig. 11). According to the Creutz–Brunschwig–Sutin model [76], it can be proposed that when the electronic coupling between a semiconductor and molecule is strong, new surface coordination species and new

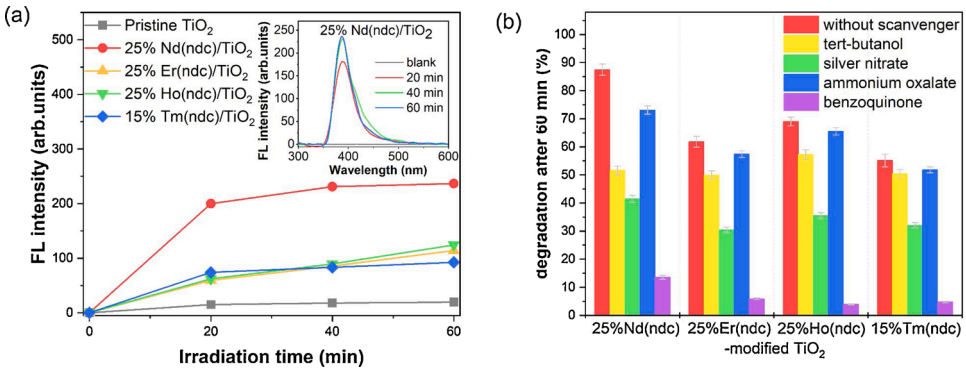

Fig. 10. (a) Fluorescence spectral changes for the terephthalic acid solution under visible light irradiation (λ> 420 nm); the insert shows the spectra of 25%Nd(ndc)/TiO_2. (b) Photocatalytic degradation under visible light irradiation (λ > 420 nm) of phenol in the presence of selected samples and scavengers.

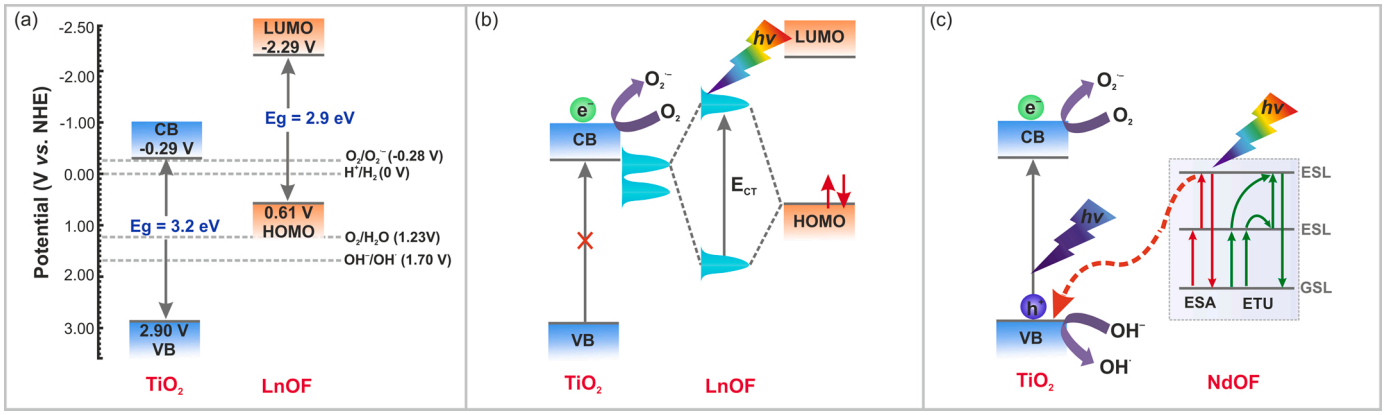

Fig. 11. (a) Schematic for band gap match in the TiO_2 and Ln(ndc) MOFs. Proposed mechanism of the excitation of Ln(ndc)-modified TiO_2 composite by visible light irradiation: (a) surface complex formed between Ln(ndc) MOF and TiO_2; (b) up-conversion pathway of Nd(ndc) MOF/TiO_2.

energy levels are formed [76]. Therefore, it can be assumed that the photoactivities of these samples are due to the formation of a charge-transfer complex between the n-type TiO_2 semiconductor and LnOF. Specifically, a binding orbital is formed between the titanium *d* orbitals of TiO_2 and the HOMO of LnOF (π aromatic orbital). While the HOMO of the LnOF system is mostly located at the molecule, the LUMO corresponds to the conduction band of TiO_2 [77]. Upon excitation of the LnOF surface complex (Fig. 11b), electron transfer is directly promoted to the LUMO localised at the titanium centres on the surface, followed by delocalization at the femtosecond timescale. The excited electron relaxes to the bottom of the conduction band, where it reacts with O_2 to produce $O_2^{\cdot-}$, further generating $^{\cdot}OH$ [35,36]. Subsequently, both $^{\cdot}OH$ and $O_2^{\cdot-}$ oxidise phenol to the by-products, and finally to carbon dioxide and water [62]. Under light irradiation, O_2 molecules can not only diffuse fast and easily into the LnOFs and undergo adsorption on the Ln^{3+} sites to form $O_2^{\cdot-}$, but also produce an oxygen-rich environment around TiO_2. This hypothesis can be explained in the difference in species trapping experiments, where superoxide radicals are the main active species produced by the Ln(ndc)/TiO_2 composites. Moreover, MOFs containing lanthanide metal ions coordinated to the oxygen of the polycarboxylic ligands trap photoexcited electrons and show considerable reduction power to drive the photocatalytic reaction. These processes are more complicated for the Nd(ndc)/TiO_2 sample. In addition to the above described mechanisms, ESA and ETU UC mechanisms are possible (Fig. 11c). Based on apparent quantum efficiency results, (provide by the action spectra analysis), it is proposed that only the MOF containing the Nd^{3+} species exhibits the up-conversion properties; this mechanism does match well with experimental results because the presence of $^{\cdot}OH$ was observed (*via* species trapping experiments). Upon the absorption of a photon, two Nd^{3+} species exchange energy such that one of the ions is further excited to an even higher energy state, while the other relaxes to a lower state. When Nd^{3+} in the excited state with energy exceeding that of the pump photon returns to the ground state, the energy can be released in the form of light with higher energy than the pump source. As shown in Fig. 11c, under continuous excitation of visible light, Nd(ndc) MOFs as UC luminescence agents likely emit UV light, which can then effectively excite TiO_2 to generate electron–hole pairs. The holes can oxidise phenol directly or react with H_2O to generate free radical species, $^{\cdot}OH$, while the electrons can react with the adsorbed O_2 to yield highly reactive $O_2^{\cdot-}$ and indirectly degrade phenol.

4. Conclusions

Novel, highly efficient, and quite stable (upon visible light irradiation) Ln(ndc)/TiO_2 photocatalysts have been successfully prepared by a versatile stepwise self-assembly strategy. The FTIR and XPS analyses confirm that the complex structure formed by the carboxylate-terminated TiO_2 and Ln(ndc) MOF is probably achieved by Ln metal ions, which are readily coordinated by 2,6-ndc for the growth of the LnOFs. In this study, the effects of different parameters, such as the type of lanthanide ions (Nd, Er, Ho, and Tm) and amount of Ln(ndc) MOFs (15, 25, and 50 wt.%), have been investigated for the evaluation of the photocatalytic behaviour. The highest efficiency of phenol degradation is achieved for 25 wt.% Nd(ndc)-modified TiO_2, affording a value of 87.5% after 60 min of visible light exposure, which is 19 times higher than that of pristine TiO_2. The combination of the antenna-reactor photocatalyst complex with Ln(ndc) shell layers promotes light harvesting and efficient mass transfer, resulting in additional photoexcited electrons. Furthermore, the Nd(ndc) MOF is shown to act as a UC luminescence agent, which can emit UV light; the AQEs at 525 and 583 nm are 2.8% and 3.2%, respectively. Energy transfer (GSA/ESA and GSA/ETU) UC is proposed as the mechanism for the observed photoactivity. The up-converted UV radiation emitted by the Nd(ndc) MOF can be absorbed by TiO_2 to generate electron–hole pairs, analogous to direct UV excitation. In addition, Er, Ho, and Tm-(ndc) MOF-modified TiO_2 are also active in the photocatalytic degradation of phenol under visible light irradiation. However, the UC process is not responsible for the activity in the visible region, probably due to electronic coupling, that is, the interaction between the LnOFs and TiO_2 surface in the form of a surface complex (charge-transfer complex between LnOFs and TiO_2). The new energy level created by the arrangement of molecular orbitals participates in electron transfer from these Ln(ndc) MOFs to the conduction band of TiO_2. Moreover, O_2 molecules can not only diffuse rapidly and easily into the LnOFs and undergo adsorption on the Ln^{3+} sites to form $O_2^{\cdot-}$, but also produce an oxygen-rich environment around TiO_2. MOFs containing lanthanide metal ions coordinated to the oxygen of the polycarboxylic ligands trap the photoexcited electrons and show a considerable reduction in power to drive the photocatalytic reaction. This study affords a new pathway for the development of novel and efficient composite photocatalysts that convert incompatible visible radiation to functional UV photons. The results are expected to be beneficial in increasing the photoactivities of the semiconductors with potential for commercial applications.

CRediT authorship contribution statement

Patrycja Parnicka: Resources, Conceptualization, Funding acquisition, Project administration, Investigation, Methodology, Visualization, Writing - original draft, Writing - review & editing. **Wojciech Lisowski:** Investigation, Visualization, Writing - original draft. **Tomasz Klimczuk:** Investigation, Visualization, Writing - original draft. **Justyna Łuczak:** Investigation, Writing - original draft. **Andrzej Żak:** Investigation, Visualization, Writing - original draft. **Adriana Zaleska-Medynska:** Resources, Supervision, Writing - review & editing.

Declaration of Competing Interest

The authors report no declarations of interest.

Acknowledgments

This research was supported by the Polish National Science Center, under the grant titled: "Novel REOF@TiO_2 nanomaterials with potential applications in photocatalytic processes", contract No.: 2017/27/N/ST5/00738.

Appendix A. Supplementary data

Supplementary material related to this article can be found, in the online version, at doi:https://doi.org/10.1016/j.apcatb.2021.120056.

References

[1] A. Zaleska-Medynska, Metal Oxide-based Photocatalysis: Fundamentals and Prospects for Application, Elsevier, 2018.
[2] P. Mazierski, A. Mikolajczyk, B. Bajorowicz, A. Malankowska, A. Zaleska-Medynska, J. Nadolna, The role of lanthanides in TiO_2-based photocatalysis: a review, Appl. Catal. B Environ. 233 (2018) 301–317, https://doi.org/10.1016/j.apcatb.2018.04.019.
[3] N.U. Saqib, R. Adnan, I. Shah, A mini-review on rare earth metal-doped TiO_2 for photocatalytic remediation of wastewater, Environ. Sci. Pollut. Res. 23 (2016) 15941–15951, https://doi.org/10.1007/s11356-016-6984-7.
[4] W. Zhang, S. Yang, J. Li, W. Gao, Y. Deng, W. Dong, C. Zhao, G. Lu, Visible-to-ultraviolet upconvertion: energy transfer, material matrix, and synthesis strategies, Appl. Catal. B Environ. 206 (2017) 89–103, https://doi.org/10.1016/j.apcatb.2017.01.023.
[5] P. Mazierski, A. Mikolajczyk, T. Grzyb, P. Nicolas Arellano Caicedo, Z. Wei, E. Kowalska, H.P. Pinto, A. Zaleska-Medynska, J. Nadolna, On the excitation mechanism of visible responsible Er -TiO_2 system proved by experimental and theoretical investigations for boosting photocatalytic activity, Appl. Surf. Sci. 527 (2020), 146815, https://doi.org/10.1016/j.apsusc.2020.146815.
[6] P. Parnicka, T. Grzyb, A. Mikolajczyk, K. Wang, E. Kowalska, N. Steinfeldt, M. Klein, P. Mazierski, A. Zaleska-medynska, J. Nadolna, Experimental and theoretical investigations of the influence of carbon on a Ho^{3+}-TiO_2 photocatalyst with vis response, J. Colloid Interface Sci. 549 (2019) 212–224, https://doi.org/10.1016/j.jcis.2019.04.074.
[7] P. Mazierski, P.N. Arellano Caicedo, T. Grzyb, A. Mikolajczyk, J.K. Roy, E. Wyrzykowska, Z. Wei, E. Kowalska, T. Puzyn, A. Zaleska-Medynska, J. Nadolna, Experimental and computational study of Tm-doped TiO_2: the effect of Li^+ on vis-response photocatalysis and luminescence, Appl. Catal. B Environ. 252 (2019) 138–151, https://doi.org/10.1016/j.apcatb.2019.03.051.
[8] P. Parnicka, P. Mazierski, T. Grzyb, Z. Wei, E. Kowalska, B. Ohtani, T. Klimczuk, J. Nadolna, Preparation and photocatalytic activity of Nd-modified TiO_2 photocatalysts: insight into the excitation mechanism under visible light, J. Catal. 353 (2017) 211–222, https://doi.org/10.1016/j.jcat.2017.07.017.
[9] Y. Liu, K. Mo, Y. Cui, Porous and robust lanthanide metal-organoboron frameworks as water tolerant Lewis acid catalysts, Inorg. Chem. 52 (2013) 10286–10291, https://doi.org/10.1021/ic400598x.
[10] N. Sabbatini, M. Guardigli, F. Bolletta, I. Manet, R. Ziessel, Luminescent Eu^{3+} and Tb^{3+} complexes of a branched macrocyclic ligand incorporating 2,2′-bipyridine in the macrocycle and phosphinate esters in the side arms, Angew. Chem. Int. Ed. Engl. 33 (1992) 1501–1503.
[11] F. Maya, C. Palomino Cabello, R.M. Frizzarin, J.M. Estela, G. Turnes Palomino, V. Cerdà, Magnetic solid-phase extraction using metal-organic frameworks (MOFs) and their derived carbons, TrAC - Trends Anal. Chem. 90 (2017) 142–152, https://doi.org/10.1016/j.trac.2017.03.004.
[12] S. Aime, M. Botta, M. Fasano, E. Terreno, Lanthanide(III) chelates for NMR biomedical applications, Chem. Soc. Rev. 27 (1998) 19–29, https://doi.org/10.1039/A827019Z.
[13] S.P. Fricker, The therapeutic application of lanthanides, Chem. Soc. Rev. 35 (2006) 524, https://doi.org/10.1039/b509608c.
[14] M. Nazari, M. Rubio-Martinez, G. Tobias, J.P. Barrio, R. Babarao, F. Nazari, K. Konstas, B.W. Muir, S.F. Collins, A.J. Hill, M.C. Duke, M.R. Hill, Metal-organic-framework-coated optical fibers as light-triggered drug delivery vehicles, Adv. Funct. Mater. 26 (2016) 3244–3249, https://doi.org/10.1002/adfm.201505260.
[15] J.J. Perry IV, C.A. Bauer, M.D. Allendorf, Luminescent metal-organic frameworks, Met. Fram. Appl. Catal. Gas Storage (2011) 267–308, https://doi.org/10.1002/9783527635856.ch12.
[16] K.K. Gangu, A.S. Dadhich, S.B. Mukkamala, Synthesis, crystal structure and fluorescent properties of two metal-organic frameworks constructed from Cd(II) and 2,6-naphthalene dicarboxylic acid, Inorg. Nano-Metal Chem. 47 (2017) 313–319, https://doi.org/10.1080/15533174.2016.1186050.
[17] P. Mahata, K.V. Ramya, S. Natarajan, Synthesis, structure and optical properties of rare-earth benzene carboxylates, Dalton Trans. 9226 (2007) 4017–4026, https://doi.org/10.1039/b706363f.
[18] P. Mahata, K.V. Ramya, S. Natarajan, Pillaring of $CdCl_2$-like layers in lanthanide metal-organic frameworks: synthesis, structure, and photophysical properties, Chem. - A Eur. J. 14 (2008) 5839–5850, https://doi.org/10.1002/chem.200800240.
[19] D. Weng, X. Zheng, X. Chen, C. Li, L. Jin, Synthesis, upconversion luminescence and magnetic properties of new lanthanide-organic frameworks with (43)2(4 6,66,83) topology, Eur. J. Inorg. Chem. 2 (2007) 3410–3415, https://doi.org/10.1002/ejic.200700140.
[20] J. Yang, Q. Yue, G.D. Li, J.J. Cao, G.H. Li, J.S. Chen, Structures, photoluminescence, up-conversion, and magnetism of 2D and 3D rare-earth coordination polymers with multicarboxylate linkages, Inorg. Chem. 45 (2006) 2857–2865, https://doi.org/10.1021/ic051557o.
[21] J.H. Pan, X.Z. Wang, Q. Huang, C. Shen, Z.Y. Koh, Q. Wang, A. Engel, D. W. Bahnemann, Large-scale synthesis of urchin-like mesoporous TiO_2 hollow spheres by targeted etching and their photoelectrochemical properties, Adv. Funct. Mater. 24 (2014) 95–104, https://doi.org/10.1002/adfm.201300946.
[22] G. Zhang, H. Sheng, D. Chen, N. Li, Q. Xu, H. Li, J. He, J. Lu, Hierarchical titanium dioxide nanowire/metal–organic framework/carbon nanofiber membranes for highly efficient photocatalytic degradation of hydrogen sulfide, Chem. A Eur. J. 24 (2018) 15019–15025, https://doi.org/10.1002/chem.201802747.
[23] N. Stock, S. Biswas, Synthesis of metal-organic frameworks (MOFs): routes to various MOF topologies, morphologies, and composites, Chem. Rev. 112 (2012) 933–969, https://doi.org/10.1021/cr200304e.
[24] J.K. Bristow, K.T. Butler, K.L. Svane, D. Gale, A. Walsh, Chemical bonding at the metal – organic framework/metal oxide interface : simulated epitaxial growth of MOF-5 on rutile TiO_2, J. Mater. Chem. A 5 (2017) 6226–6232, https://doi.org/10.1039/c7ta00356k.
[25] P. Parnicka, A. Zaleska-medynska, The effect of the metal type on luminescence and photocatalytic properties of lanthanide–organic frameworks–modified titania, Proceedings 16 (1) (2019), https://doi.org/10.3390/proceedings2019016011.
[26] L.S.S. Ramirez, S.R. Gentile, S. Zimmermann, Behavior of TiO_2 and CeO_2 nanoparticles and polystyrene nanoplastics in bottled mineral, drinking and lake Geneva waters. Impact of water hardness and natural organic matter on nanoparticle surface properties and aggregation, Water 11 (2019) 1–14, https://doi.org/10.3390/w11040721.
[27] J. Xie, X. Pan, M. Wang, J. Ma, Y. Fei, P. Wang, L. Mi, The role of surface modification for TiO_2 nanoparticles in cancer cells, Colloids Surf. B Biointerfaces 143 (2016) 148–155, https://doi.org/10.1016/j.colsurfb.2016.03.029.
[28] Z. Yuan, L. Zhang, S. Li, W. Zhang, M. Lu, Y. Pan, X. Xie, L. Huang, W. Huang, Paving metal-organic frameworks with upconversion nanoparticles via self-assembly, J. Am. Chem. Soc. 140 (2018) 15507–15515, https://doi.org/10.1021/jacs.8b10122.
[29] P. Parnicka, P. Mazierski, W. Lisowski, T. Klimczuk, J. Nadolna, A. Zaleska-Medynska, A new simple approach to prepare rare-earth metals-modified TiO_2nanotube arrays photoactive under visible light: surface properties and mechanism investigation, Results Phys. 12 (2019) 412–423, https://doi.org/10.1016/j.rinp.2018.11.073.
[30] C.-C. Wang, C.-T. Yeh, S.-Y. Ke, Y.-T. Cheng, C.-C. Yang, G.-H. Lee, C.-K. Chang, H.-S. Sheu, Assembly of three Nd(III) 2,6-naphthalenedicarboxylates (ndc^{2-}) 3D coordination polymers based on various secondary building units (SBUs): structural diversity and gas sorption properties, RSC Adv. 5 (2015) 92378–92386, https://doi.org/10.1039/c5ra10799g.
[31] A. Kula, Thermal and luminescence characterization of lanthanide 2,6-naphthalenedicarboxylates series, J. Anal. Appl. Pyrolysis 92 (2011) 347–354, https://doi.org/10.1016/j.jaap.2011.07.006.
[32] R. Łyszczek, A. Lipke, Microwave-assisted synthesis of lanthanide 2,6-naphthalenedicarboxylates: thermal, luminescent and sorption characterization, Microporous Mesoporous Mater. 168 (2013) 81–91, https://doi.org/10.1016/j.micromeso.2012.09.016.
[33] A. León, P. Reuquen, C. Garín, R. Segura, P. Vargas, P. Zapata, P.A. Orihuela, FTIR and raman characterization of TiO_2 nanoparticles coated with polyethylene glycol as carrier for 2-methoxyestradiol, Appl. Sci. 7 (2017) 1–9, https://doi.org/10.3390/app7010049.
[34] H. Matsuyoshi, S. Kawasaki, K. Yamada, H. Nishimura, Effects of cycloalkylcarboxylic acid derivatives as coadsorbents on the photovoltaic performance of dye-sensitized solar cells, Annu. Tech. Conf. - ANTEC, Conf. Proc. 0 (2015) 758–762.
[35] A. Buhori, A. Zulys, J. Gunlazuardi, Synthesis of lanthanum metal-organic frameworks (La-MOFs) as degradation photocatalyst of Rhodamine-B, AIP Conf. Proc. 2242 (2020), https://doi.org/10.1063/5.0013010.
[36] A. Nasruddin, Zulys, F. Yulia, A. Buhori, N. Muhadzib, M. Ghiyats, B.B. Saha, Synthesis and characterization of a novel microporous lanthanide based metal-organic framework (MOF) using napthalenedicarboxylate acid, J. Mater. Res. Technol. 9 (2020) 7409–7417, https://doi.org/10.1016/j.jmrt.2020.05.015.
[37] B. Farkaš, U. Terranova, N.H. De Leeuw, Binding modes of carboxylic acids on cobalt nanoparticles, Phys. Chem. Chem. Phys. 22 (2020) 985–996, https://doi.org/10.1039/c9cp04485j.
[38] Y. Ma, Y. Lu, G. Hai, W. Dong, R. Li, J. Liu, G. Wang, Bidentate carboxylate linked TiO_2 with NH_2-MIL-101(Fe) photocatalyst: a conjugation effect platform for high photocatalytic activity under visible light irradiation, Sci. Bull. 65 (2020) 658–669, https://doi.org/10.1016/j.scib.2020.02.001.
[39] M. Zhang, Q. Shang, Y. Wan, Q. Cheng, G. Liao, Z. Pan, Self-template synthesis of double-shell TiO_2@ZIF-8 hollow nanospheres via sonocrystallization with enhanced photocatalytic activities in hydrogen generation, Appl. Catal. B Environ. 241 (2019) 149–158, https://doi.org/10.1016/j.apcatb.2018.09.036.

[40] H. Sheng, D. Chen, N. Li, Q. Xu, H. Li, J. He, J. Lu, Urchin-Inspired TiO_2@MIL-101 Double-Shell Hollow Particles: Adsorption and Highly Efficient Photocatalytic Degradation of Hydrogen Sulfide, Chem. Mater. 29 (2017) 5612–5616, https://doi.org/10.1021/acs.chemmater.7b01243.

[41] A.V. Naumkin, A. Kraut-Vass, C.J. Powell, S.W. Gaarenstroom, National Institute of Standards and Technology (U.S.), NIST X-ray photoelectron spectroscopy database, 2012. http://srdata.nist.gov/xps/Default.aspx.

[42] F. Tian, A.M. Cerro, A.M. Mosier, H.K. Wayment-Steele, R.S. Shine, A. Park, E. R. Webster, L.E. Johnson, M.S. Johal, L. Benz, Surface and stability characterization of a nanoporous ZIF-8 thin film, J. Phys. Chem. C. 118 (2014) 14449–14456, https://doi.org/10.1021/jp5041053.

[43] A.T. Yurii, T. Anton Yu, Structure of X-ray photoelectron spectra of lanthanide compounds, Russ. Chem. Rev. 71 (2002) 347, https://doi.org/10.1070/RC2002v071n05ABEH000717.

[44] J. Reszczyńska, T. Grzyb, J.W. Sobczak, W. Lisowski, M. Gazda, B. Ohtani, A. Zaleska, Visible light activity of rare earth metal doped (Er^{3+}, Yb^{3+} or Er^{3+}/Yb^{3+}) titania photocatalysts, Appl. Catal. B Environ. 163 (2015) 40–49, https://doi.org/10.1016/j.apcatb.2014.07.010.

[45] T.-M. Pan, C.-H. Lu, S. Mondal, F.-H. Ko, Resistive switching characteristics of Tm_2O_3, Yb_2O_3, and Lu_2O_3-based metal–insulator–metal memory devices, IEEE Trans. Nanotechnol. 11 (2012) 1040–1046, https://doi.org/10.1109/TNANO.2012.2211893.

[46] A.V. Naumkin, A. Kraut-Vass, S.W. Gaarenstroom, C.J. Powell, NIST Standard Reference Database 20, Version 4.1, 2012, https://doi.org/10.18434/T4T88K. http://srdata.nist.gov/xps/).

[47] J. Bedia, V. Muelas-Ramos, M. Peñas-Garzón, A. Gómez-Avilés, J.J. Rodríguez, C. Belver, A review on the synthesis and characterization of metal organic frameworks for photocatalytic water purification, Catalysts 9 (2019), https://doi.org/10.3390/catal9010052.

[48] A.-W. Xu, Y. Gao, H.-Q. Liu, The preparation, characterization, and their photocatalytic activities of rare-earth-doped TiO_2 nanoparticles, J. Catal. 207 (2002) 151–157, https://doi.org/10.1006/jcat.2002.3539.

[49] M.I.M. Zamratul, W.A. Zaidan, A.M. Khamirul, S.A. Halim, S.A. Raba'ah, M. Nurzilla, B.P. Nur Fadilah, Novel eco-friendly synthesis of neodymium doped zinc silicate phosphor based waste glass ceramic: structural, thermal and luminescence properties, J. Mater. Sci. Mater. Electron. 28 (2017) 9395–9402, https://doi.org/10.1007/s10854-017-6680-5.

[50] V.C. Bhethanabotla, D.R. Russell, J.N. Kuhn, Assessment of mechanisms for enhanced performance of Yb/Er/titania photocatalysts for organic degradation: role of rare earth elements in the titania phase, Appl. Catal. B Environ. 202 (2017) 156–164, https://doi.org/10.1016/j.apcatb.2016.09.008.

[51] S. Obregón, A. Kubacka, M. Fernández-García, G. Colón, High-performance Er^{3+}-TiO_2 system: dual up-conversion and electronic role of the lanthanide, J. Catal. 299 (2013) 298–306, https://doi.org/10.1016/j.jcat.2012.12.021.

[52] K. Das, V. Nagarajan, M.L. Nandagoswami, D. Panda, A. Dhar, S.K. Ray, Optical characteristics of Er^{3+}-doped Ge nanocrystals in sol-gel-derived SiO_2 glass, Nanotechnology 18 (2007), https://doi.org/10.1088/0957-4484/18/9/095704.

[53] T. Ragin, J. Zmojda, M. Kochanowicz, P. Miluski, R. Jadach, M. Sitarz, D. Dorosz, J. Dorosz, Spectroscopic properties and energy transfer in Er/Ag co-doped antimony oxide glass, Photonics Appl. Astron. Commun. Ind. High Energy Phys. Exp. 10445 (2017) (2017), 104454V, https://doi.org/10.1117/12.2280278.

[54] B. Karmakar, IRRS, UV-Vis-NIR absorption and photoluminescence upconversion in Ho^{3+}-doped oxyfluorophosphate glasses, J. Solid State Chem. 178 (2005) 2663–2672, https://doi.org/10.1016/j.jssc.2005.06.007.

[55] P. Peterka, I. Kasik, A. Dhar, B. Dussardier, W. Blanc, Theoretical modeling of fiber laser at 810 nm based on thulium-doped silica fibers with enhanced $^3H_4$ level lifetime, Opt. Express 19 (2011) 2773, https://doi.org/10.1364/oe.19.002773.

[56] M.T. Pinho, H.T. Gomes, R.S. Ribeiro, J.L. Faria, A.M.T. Silva, Carbon nanotubes as catalysts for catalytic wet peroxide oxidation of highly concentrated phenol solutions: towards process intensification, Appl. Catal. B Environ. 165 (2015) 706–714, https://doi.org/10.1016/j.apcatb.2014.10.057.

[57] C. Zhao, X. Pan, Z. Wang, C. Wang, 1+1&2: a critical review of MOF/bismuth-based semiconductor composites for boosted photocatalysis, Chem. Eng. J. (2020), 128022, https://doi.org/10.1016/j.cej.2020.128022.

[58] J. Zhang, Y. Hu, J. Qin, Z. Yang, M. Fu, TiO_2-UiO-66-NH_2 nanocomposites as efficient photocatalysts for the oxidation of VOCs, Chem. Eng. J. 385 (2020), 123814, https://doi.org/10.1016/j.cej.2019.123814.

[59] A. Crake, K.C. Christoforidis, A. Kafizas, S. Zafeiratos, C. Petit, CO_2 capture and photocatalytic reduction using bifunctional TiO_2/MOF nanocomposites under UV–vis irradiation, Appl. Catal. B Environ. 210 (2017) 131–140, https://doi.org/10.1016/j.apcatb.2017.03.039.

[60] Q. Liu, B. Zhou, M. Xu, G. Mao, Integration of nanosized ZIF-8 particles onto mesoporous TiO_2 nanobeads for enhanced photocatalytic activity, RSC Adv. 7 (2017) 8004–8010, https://doi.org/10.1039/C6RA28277F.

[61] I. Wysocka, E. Kowalska, K. Trzciński, M. Łapiński, G. Nowaczyk, A. Zielińska-Jurek, UV-Vis-induced degradation of phenol over magnetic photocatalysts modified with Pt, Pd, Cu and Au nanoparticles, Nanomaterials 8 (2018), https://doi.org/10.3390/nano8010028.

[62] T.T.T. Dang, S.T.T. Le, D. Channei, W. Khanitchaidecha, A. Nakaruk, Photodegradation mechanisms of phenol in the photocatalytic process, Res. Chem. Intermed. 42 (2016) 5961–5974, https://doi.org/10.1007/s11164-015-2417-3.

[63] Z. Wu, Y. Wang, Z. Xiong, Z. Ao, S. Pu, G. Yao, B. Lai, Core-shell magnetic Fe_3O_4@Zn/Co-ZIFs to activate peroxymonosulfate for highly efficient degradation of carbamazepine, Appl. Catal. B Environ. 277 (2020), 119136, https://doi.org/10.1016/j.apcatb.2020.119136.

[64] Y. Zhang, Y. Zhao, Z. Xiong, T. Gao, B. Gong, P. Liu, J. Liu, J. Zhang, Elemental mercury removal by I−-doped Bi_2WO_6 with remarkable visible-light-driven photocatalytic oxidation, Appl. Catal. B Environ. 282 (2021), 119534, https://doi.org/10.1016/j.apcatb.2020.119534.

[65] Q. Ma, H. Zhang, X. Zhang, B. Li, R. Guo, Q. Cheng, X. Cheng, Synthesis of magnetic CuO/$MnFe_2O_4$ nanocompisite and its high activity for degradation of levofloxacin by activation of persulfate, Chem. Eng. J. 360 (2019) 848–860, https://doi.org/10.1016/j.cej.2018.12.036.

[66] Q. Sun, H. He, W.Y. Gao, B. Aguila, L. Wojtas, Z. Dai, J. Li, Y.S. Chen, F.S. Xiao, S. Ma, Imparting amphiphobicity on single-crystalline porous materials, Nat. Commun. 7 (2016) 1–7, https://doi.org/10.1038/ncomms13300.

[67] A. Nadort, J. Zhao, E.M. Goldys, Lanthanide upconversion luminescence at the nanoscale: fundamentals and optical properties, Nanoscale 8 (2016) 13099–13130, https://doi.org/10.1039/C5NR08477F.

[68] M. Safdar, A. Ghazy, M. Lastusaari, M. Karppinen, Lanthanide-based inorganic-organic hybrid materials for photon-upconversion, J. Mater. Chem. C 8 (2020) 6946–6965, https://doi.org/10.1039/d0tc01216e.

[69] P.J. Dihingia, S. Rai, Synthesis of TiO_2 nanoparticles and spectroscopic upconversion luminescence of Nd^{3+}-doped TiO_2-SiO_2 composite glass, J. Lumin. 132 (2012) 1243–1251, https://doi.org/10.1016/j.jlumin.2011.12.008.

[70] O. Ola, M.M. Maroto-Valer, Review of material design and reactor engineering on TiO_2 photocatalysis for CO_2 reduction, J. Photochem. Photobiol. C Photochem. Rev. 24 (2015) 16–42, https://doi.org/10.1016/j.jphotochemrev.2015.06.001.

[71] M. Klein, J. Nadolna, A. Gołabiewska, P. Mazierski, T. Klimczuk, H. Remita, A. Zaleska-Medynska, The effect of metal cluster deposition route on structure and photocatalytic activity of mono- and bimetallic nanoparticles supported on TiO_2 by radiolytic method, Appl. Surf. Sci. 378 (2016) 37–48, https://doi.org/10.1016/j.apsusc.2016.03.191.

[72] P. Parnicka, P. Mazierski, T. Grzyb, W. Lisowski, E. Kowalska, B. Ohtani, A. Zaleska-Medynska, J. Nadolna, Influence of the preparation method on the photocatalytic activity of Nd-modified TiO_2, Beilstein J. Nanotechnol. 9 (2018) 447–459, https://doi.org/10.3762/bjnano.9.43.

[73] D.C. Ghosh, T. Chakraborty, Gordy's electrostatic scale of electronegativity revisited, J. Mol. Struct. Theochem. 906 (2009) 87–93, https://doi.org/10.1016/j.theochem.2009.04.007.

[74] R. Li, W. Zhang, K. Zhou, Metal–organic-framework-based catalysts for photoreduction of CO_2, Adv. Mater. 30 (2018) 1–31, https://doi.org/10.1002/adma.201705512.

[75] N.H. Batubara, A. Zulys, Synthesis, structural, spectroscopic, and morphology of metal-organic frameworks based on La (III) and ligand 2,6-Napthalenedicarboxylic acid (La-MOFs) for hydrogen production, IOP Conf. Ser. Mater. Sci. Eng. 546 (2019), https://doi.org/10.1088/1757-899X/546/4/042005.

[76] C. Creutz, B.S. Brunschwig, N. Sutin, Interfacial charge-transfer absorption: 3. Application to semiconductor - molecule assemblies, J. Phys. Chem. B 110 (2006) 25181–25190, https://doi.org/10.1021/jp063953d.

[77] P. Kwolek, M. Oszajca, K. Szaciłowski, Catecholate and 2,3-acenediolate complexes of d° ions as prospective materials for molecular electronics and spintronics, Coord. Chem. Rev. 256 (2012) 1706–1731, https://doi.org/10.1016/j.ccr.2012.03.028.